ARTICLE OPEN

Check for updates

Pitolisant alleviates brain network dysfunction and cognitive deficits in a mouse model of Alzheimer's disease

Yang Zou[1], Linhan Yang[1], Jiahui Zhu[1], Jihua Fan[1], Hanrun Zheng[2], Xiang Liao[3], Zhiqi Yang[4], Kuan Zhang[4,5,6], Hongbo Jia[1,7,8,9], Arthur Konnerth[7], Yan-jiang Wang[5,6], Chunqing Zhang[5,6]✉, Yun Zhang[2]✉, Sunny C. Li[6,10]✉ and Xiaowei Chen[4,5,6]✉

Histamine H_3 receptor (H_3R) antagonists regulate histamine release that modulates neuronal activity and cognitive function. Although H_3R is elevated in Alzheimer's disease (AD) patients, whether H_3R antagonists can rescue AD-associated neural impairments and cognitive deficits remains unknown. Pitolisant is a clinically approved H_3R antagonist/inverse agonist that treats narcolepsy. Here, we find that pitolisant reverses AD-like pathophysiology and cognitive impairments in an AD mouse model. Behavioral assays and in vivo wide-field Ca^{2+} imaging revealed that recognition memory, learning flexibility, and slow-wave impairment were all improved following the 15-day pitolisant treatment. Improved recognition memory was tightly correlated with slow-wave coherence, suggesting slow waves serve as a biomarker for treatment response and for AD drug screening. Furthermore, pitolisant reduced amyloid-β deposition and dystrophic neurites surrounding plaques, and enhanced neuronal lysosomal activity, inhibiting which blocked cognitive and slow-wave restoration. Our findings identify pitolisant as a potential therapeutic agent for AD treatments.

Translational Psychiatry (2025)15:126 ; https://doi.org/10.1038/s41398-025-03358-8

INTRODUCTION

Alzheimer's disease (AD) is a progressive neurodegenerative disorder, primarily characterized by a gradual decline in cognitive function [1]. The most typical pathological hallmark of AD is amyloid-beta (Aβ) plaques [1]. In recent years, numerous monoclonal antibodies targeting brain Aβ have entered clinical trials. Among them, donanemab and lecanemab [2, 3] have shown remarkable efficacy in clearing Aβ plaques from the brain of AD patients. However, the improvement in cognitive abilities is limited [4–6], as they might not reverse the neuronal impairments that have occurred widely in the brain networks. Clearly, lessons learned from these clinical trials suggest that a strategy solely targeting Aβ clearance does not fully correlate with improvements in patients' cognitive function [7].

Recent accumulating evidence suggests a direct link between disruption of neuronal network and cognitive impairment in AD, largely based on two lines of evidence obtained from animal model studies. On the cellular level, two-photon Ca^{2+} imaging experiments indicate that neurons in the hippocampus and cortex are hyperactive in AD or even at the early stage of AD [8, 9]. On the network level, wide-field Ca^{2+} imaging studies have shown that cortical slow waves (slow oscillations; i.e., low-frequency, high-amplitude oscillations in the frequency range of 0.1 to 3 Hz [10]) are disrupted in anesthetized APP/PS1 AD model mice [11]. Importantly, this work also reported that restoration of normal neuronal network activity occurs conjointly with the rescue of cognitive disruption in AD mice [11]. Slow waves are present during non-rapid eye movement (NREM) sleep as well, and are suggested to be associated with memory consolidation [12, 13], clearance of metabolic waste in the brain [14–16], and neural cell repair [17]. In AD patients, slow waves are also impaired [18, 19]. Unsurprisingly, neuronal dysfunction was shown to be associated with network disruption, ultimately resulting in cognitive deficits in learning and memory [20]. It is, therefore, necessary to screen new candidate drugs that can restore neuronal network function to improve cognitive functions in AD.

H_3R is a histamine G protein-coupled receptor (GPCR) that is primarily expressed in the brain [21] and regulates histamine release to modulate neuronal activity and influence various cognitive functions [21]. Pitolisant is the first H_3R antagonist/inverse agonist that has been approved to treat narcolepsy [22]. Clinical studies have found that H_3R expression is higher in AD patients [23]. H_3R inverse agonists have been shown to enhance long-term memory performance in both mice and healthy adult humans [24], but it currently remains unclear whether pitolisant can benefit AD patients. Here, we found that the 15-day pitolisant

[1]Guangxi Key Laboratory of Special Biomedicine/Advanced Institute for Brain and Intelligence, School of Medicine, Guangxi University, Nanning 530004, China. [2]State Key Laboratory of Structural Chemistry, Fujian Institute of Research on the Structure of Matter, Chinese Academy of Sciences, Fuzhou 350002, China. [3]Center for Neurointelligence, School of Medicine, Chongqing University, Chongqing 400044, China. [4]Brain Research Center and State Key Laboratory of Trauma and Chemical Poisoning, Third Military Medical University, Chongqing 400038, China. [5]Institute of Brain and Intelligence, Third Military Medical University, Chongqing 400038, China. [6]LFC Laboratory and Chongqing Institute for Brain and Intelligence, Guangyang Bay Laboratory, Chongqing 400064, China. [7]Institute of Neuroscience and Munich Cluster for Systems Neurology, Technical University Munich, 80802 Munich, Germany. [8]Combinatorial NeuroImaging Core Facility, Leibniz Institute for Neurobiology, 39118 Magdeburg, Germany. [9]Brain Research Instrument Innovation Center, Suzhou Institute of Biomedical Engineering and Technology, Chinese Academy of Sciences, Suzhou 215163, China. [10]NewLight Neuroscience Unit, Chongqing 400064, China. ✉email: cqzhang@tmmu.edu.cn; zhangy@fjirsm.ac.cn; sunnycli@lotos2.com; xiaowei_chen@tmmu.edu.cn

Received: 2 August 2024 Revised: 16 March 2025 Accepted: 27 March 2025
Published online: 05 April 2025

treatment significantly improved learning and memory performance, and rescued cortical slow-wave impairment in a β-amyloidosis mouse model. Pharmacological experiments have shown that neuronal lysosomal function may underlie the mechanism of pitolisant-mediated improvement in cortical slow-wave activity and cognitive abilities. This work provides a potential target for neuroprotection through up-regulating lysosomal function [7] that rescues the dysfunction of neural networks to improve the patients' quality of life and interrupt the progression of AD.

RESULT

Pitolisant rescues cognitive impairments in 5xFAD mice

We investigated the behavioral impairments in transgenic 5xFAD mice, an animal model of AD in which Aβ is elevated to pathological levels in the brain with cognitive deficits [25]. To determine whether chronic treatment with pitolisant could improve cognitive functions in 5xFAD mice, we tested non-spatial/spatial recognition memory in male 5xFAD mice given 15 days of treatment with saline or pitolisant (20 mg/kg/d) using the novel object recognition test (NORT) or novel object location recognition test (NLRT) (Fig. 1a, c). During the learning phase in NORT, no differences were observed in mouse recognition index (see Methods) with objects among the pitolisant- or saline-treated 5xFAD or wild-type (WT) control groups (Fig. 1b left), indicating that these mice displayed no discernible preference for any of the test objects. However, upon presentation of a novel object during the testing phase, the saline-treated 5xFAD group spent less time exploring the object than the saline-treated WT mice (Fig. 1b right), suggesting that object recognition memory was indeed impaired in the 5xFAD vehicle control group. By contrast, 5xFAD mice treated with pitolisant spent significantly more time exploring the novel object than the 5xFAD vehicle control group (Fig. 1b right), suggesting that object recognition (i.e., memory) was improved in mice treated with pitolisant. Similar to these results, 15-day pitolisant treatment resulted in an enhanced interaction index of time spent with previously introduced objects moved to a novel location in 5xFAD mice compared with their saline-treated 5xFAD counterparts (Fig. 1d), suggesting improvement of the impaired spatial memory (between groups). To further eliminate the potential confounding effects of variability among individual animals in baseline cognitive ability, we modified the experimental paradigm (Fig. 1e, g) to assess changes in cognitive ability in the same mice pre- and post-pitolisant administration (within groups). The results of NORT showed that cognitive abilities were significantly enhanced in the same 5xFAD mice after pitolisant treatment compared to their pre-administration baseline performance (Fig. 1f), which was also observed in the NLRT (Fig. 1h).

We also administrated acute experiments with a dose of pitolisant (20, 50 or 100 mg/kg) in 5xFAD mice and then conducted the NORT task. We found no significant changes in cognitive abilities, as compared to the control group (Supplementary Figure 1). In addition, we tested the cognitive impacts of chronic pitolisant treatment at different doses (0.1, 1, 5, 10, 20 mg/kg) in 5xFAD mice (Fig. 1i, j). The results of NORT or NLRT revealed that the low doses (0.1–1 mg/kg) of pitolisant did not significantly alter non-spatial or spatial memory in 5xFAD mice, whereas 5xFAD mice treated with the higher doses (10, 20 mg/kg) showed enhanced cognitive ability, suggesting that the cognitive effects of pitolisant are dose-dependent.

To test the impact of long-term pitolisant treatment on learning behavior in WT mice, we investigated the cognitive abilities of WT mice by administrating either saline or 20 mg/kg/d pitolisant for 15 days (Supplementary Figure 2a, e). In NORT, we designed two-delay conditions: one with a 10-minutes delay (Supplementary Figure 2b) and another with a 24-hour delay (Supplementary Figure 2c). The NORT results indicated no significant difference in the interaction index with the novel object between WT mice treated with long-term pitolisant and the saline control group, nor between male and female mice (Supplementary Figure 2d). The NLRT also included two-delay conditions (Supplementary Figure 2f, g). Similar to the NORT results, the interaction index with previously introduced objects moved to a new location showed no significant difference between WT mice treated with long-term pitolisant and the control group, nor between females and males (Supplementary Figure 2h). These data suggest that pitolisant does not affect learning and memory tested in WT mice.

Pitolisant restores synchronization of cortical slow waves in 5xFAD mice

To characterize the effect of pitolisant on neuronal activity across the cortical network, we used wild-field imaging to monitor Ca^{2+} fluorescence signals with a high-speed scientific complementary metal-oxide-semiconductor (sCMOS) camera in mice under anesthesia with isoflurane (0.8–1.0%) (Supplementary Figure 3a left). We exposed both hemispheres by making a large craniotomy (Supplementary Figure 3a center left), followed by bulk loading of cortical tissues with the Ca^{2+} indicator, Cal-520-AM (Supplementary Figure 3a center right) in multiple locations (Supplementary Figure 3a right). Consistent with previous studies, isoflurane anesthesia induced slow waves under 1 Hz which is similar to those occurring during natural NREM sleep [10]. The Ca^{2+} signals represent an aggregate of neuronal and neuropil activity [11, 26, 27]. To quantify the cortex-wide spatiotemporal patterns of slow-wave activity, we divided each hemisphere into four regions, from anterior to posterior: the frontal cortex, the motor cortex, the somatosensory cortex, and the occipital cortex (Supplementary Figure 3a right) [11]. Synchronization of these regions was then determined by correlation analysis, with strong correlations (i.e., high coherence close to 1 between signals) indicating synchronization and no correlation (i.e., low coherence close to 0 between signals) indicating out of phase in signaling across the cortex.

In wide-field Ca^{2+} imaging experiments of WT mice treated with saline for 15 days, slow-wave activity exhibited highly consistent Ca^{2+} signal patterns within each region, matching the signaling traces recorded in other regions (Fig. 2a, b). However, wide-field Ca^{2+} imaging experiments in male 5xFAD mice treated with saline for 15 days showed that slow-wave activity followed a relatively disorganized pattern of Ca^{2+} signals in each region that did not match signaling traces recorded in other regions, indicating a breakdown of coherence in 5xFAD mice (Fig. 2c, d). Strikingly, such disruption of cortical synchronization was significantly rescued by pitolisant, as slow-wave activity showed increasing regularity and shared higher correlation among regions in 5xFAD mice treated with pitolisant (Fig. 2e, f), which were more similar to patterns observed in saline-treated WT mice (Fig. 2a, b).

To quantify the difference between different groups, we plotted the coherence of signals as a function of the distance between brain regions ("near" = two neighboring cortical regions; "mid" = separated by one region; "far" = separated by two regions (i.e., between occipital and frontal cortex) [11]. In WT mice, the coherence was high and only showed a small decrease with distance. In 5xFAD mice, the coherence was markedly lower than those in WT mice, especially between cortical regions that were separated by longer distances. In pitolisant-treated 5xFAD mice, the coherence was higher among near, mid and far regions than vehicle control 5xFAD mice. A two-way analysis of variance (ANOVA) showed that difference between groups were highly significant (Fig. 2g). Likewise, the frequency of slow waves in different regions of pitolisant-treated 5xFAD mice was also more similar to that of vehicle-treated WT mice than to vehicle-treated 5xFAD mice (Fig. 2h), indicating that both breakdown of synchronization and increased frequency observed in the AD mouse model were rescued by 15-day pitolisant treatment.

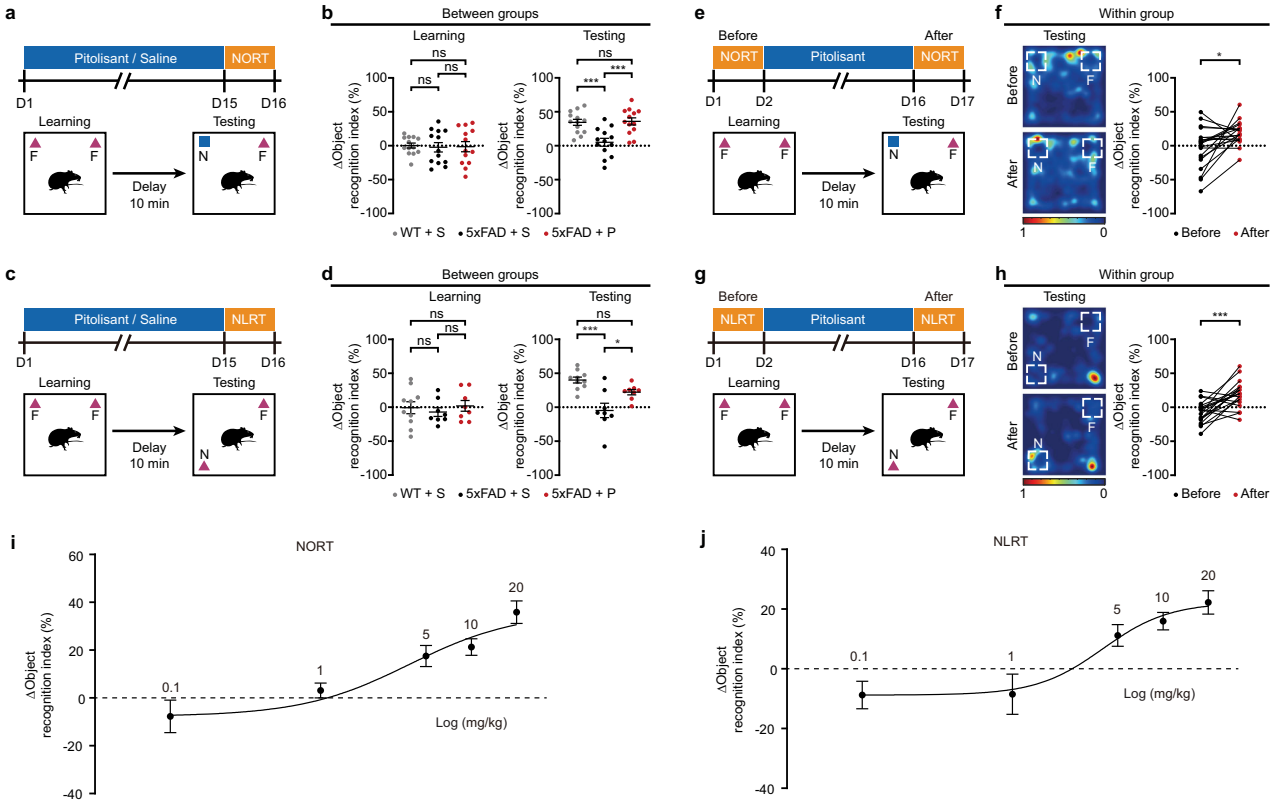

Fig. 1 Pitolisant significantly improves recognition memory in 5xFAD mice. a Unpaired experimental procedure for pitolisant treatment (top) and novel object recognition test (NORT, bottom) executed for 5xFAD mice after treatment (20 mg/kg pitolisant or same volume of saline per day for 15 days; male mice 6 to 7 months of age; F = familiar, N = novel). **b** Statistic plots showing results from the unpaired NORT procedure. Left: Statistic plot of the NORT learning phase (n = 13 WT mice with saline; n = 13 5xFAD mice with saline; n = 13 5xFAD mice with 20 mg/kg pitolisant; Welch ANOVA with Dunnett's T3 multiple comparisons test; WT + saline (S) versus 5xFAD + S, $P = 0.9830$; WT + S versus 5xFAD + pitolisant (P), $P = 0.9965$; 5xFAD + S versus 5xFAD + P, $P = 0.9996$). Right: Statistic plot of the NORT testing phase (n = 13 WT mice with saline; n = 13 5xFAD mice with saline; n = 13 5xFAD mice with 20 mg/kg pitolisant; one-way ANOVA with Tukey's multiple comparisons test, WT + S versus 5xFAD + S, $P = 0.0008$; WT + S versus 5xFAD + P, $P = 0.9814$; 5xFAD + S versus 5xFAD + P, $P = 0.0005$). **c** Unpaired experimental procedure for pitolisant treatment (top) and novel location recognition test (NLRT, bottom) executed for 5xFAD mice after treatment (20 mg/kg pitolisant or same volume of saline per day for 15 days; male mice 6 to 7 months of age; F = familiar, N = novel). **d** Statistic plots showing results from the unpaired NLRT procedure. Left: Statistic plot of the NLRT learning phase (n = 10 WT mice with saline; n = 8 5xFAD mice with saline; n = 8 5xFAD mice with 20 mg/kg pitolisant; one-way ANOVA with Tukey's multiple comparisons test; WT + S versus 5xFAD + S, $P = 0.8337$; WT + S versus 5xFAD + P, $P = 0.9698$; 5xFAD + S versus 5xFAD + P, $P = 0.724$). Right: Statistic plot of the NORT testing phase (n = 10 WT mice with saline; n = 8 in 5xFAD mice with saline; n = 8 5xFAD mice with 20 mg/kg pitolisant; one-way ANOVA with Tukey's multiple comparisons test; WT + S versus 5xFAD + S, $P = 0.0002$; WT + S versus 5xFAD + P, $P = 0.1551$; 5xFAD + S versus 5xFAD + P, $P = 0.0293$). **e** Paired experimental procedure for pitolisant treatment (top) and novel object recognition test (NORT, bottom) executed for 5xFAD mice before and after treatment (20 mg/kg per day for 15 days; male mice 6 to 7 months of age; F = familiar, N = novel). **f** Heat-map plots showing object recognition memory measures during the testing phase from NORT. The statistic plot shows the Δobject recognition index during the testing phase of NORT (n = 20 mice; two-tailed paired *t*-test; $P = 0.0113$). **g** Paired experimental procedure for pitolisant treatment (top) and novel location recognition test (NLRT, bottom) (20 mg/kg per day for 15 days; male mice 6 to 7 months of age). **h** heat-map plots showing Δobject recognition memory measures in the testing phase from NLRT. The statistic plot shows the cognition index during the testing phase of NLRT (n = 20 mice; two-tailed paired *t*-test; $P = 0.0002$). **i** Fitted dose-dependent curve for 5xFAD after pitolisant treatment in NORT. **j** Fitted dose-dependent curve for 5xFAD after pitolisant treatment in NLRT. Each dot represents an individual animal. Error bars represent mean ± SEM. $^*P < 0.05$, $^{**}P < 0.01$, $^{***}P < 0.001$, ns = no significance.

Furthermore, we found that the coherence of slow-wave activity was significantly correlated with cognitive behavioral performance in NORT (Fig. 2i) or NLRT (Fig. 2j) assays. These results suggest that slow-wave activity in the cortex could serve as a biomarker for drug efficacy in the evaluation of brain network function and cognitive ability. We also examined the effects of acute pitolisant (20 mg/kg, one dose) administration on slow-wave activity through large-scale Ca^{2+} imaging experiments (Supplementary Figure 3b, e). We found that such single-dose pitolisant treatment had no effect on the coherence of cortical activity (Supplementary Figure 3c, f) or frequency of Ca^{2+} signals (Supplementary Figure 3d, g) in either in 5xFAD or WT mice, indicating that acute pitolisant administration did not affect slow-wave activity.

Additionally, we conducted experiments at different treatment time points to assess cognitive abilities and neural network changes (Supplementary Figure 4a–c). The results showed that administration of pitolisant for 3, 5, or 10 days did not significantly affect slow-wave oscillations (Supplementary Figure 4d, e) and cognitive abilities (Supplementary Figure 4f, g) in 5xFAD mice.

Pitolisant rescues impaired cognitive flexibility in 5xFAD mice

The ability of an individual to quickly adjust their behavior strategies when faced with changing environments (or cognitive flexibility) is often impaired in AD patients [28–31]. To investigate whether pitolisant could affect spatial cognitive flexibility, we tested our treatment groups in a modified Morris water maze [32] (Fig. 3a; see Methods). After several days of training, all mice

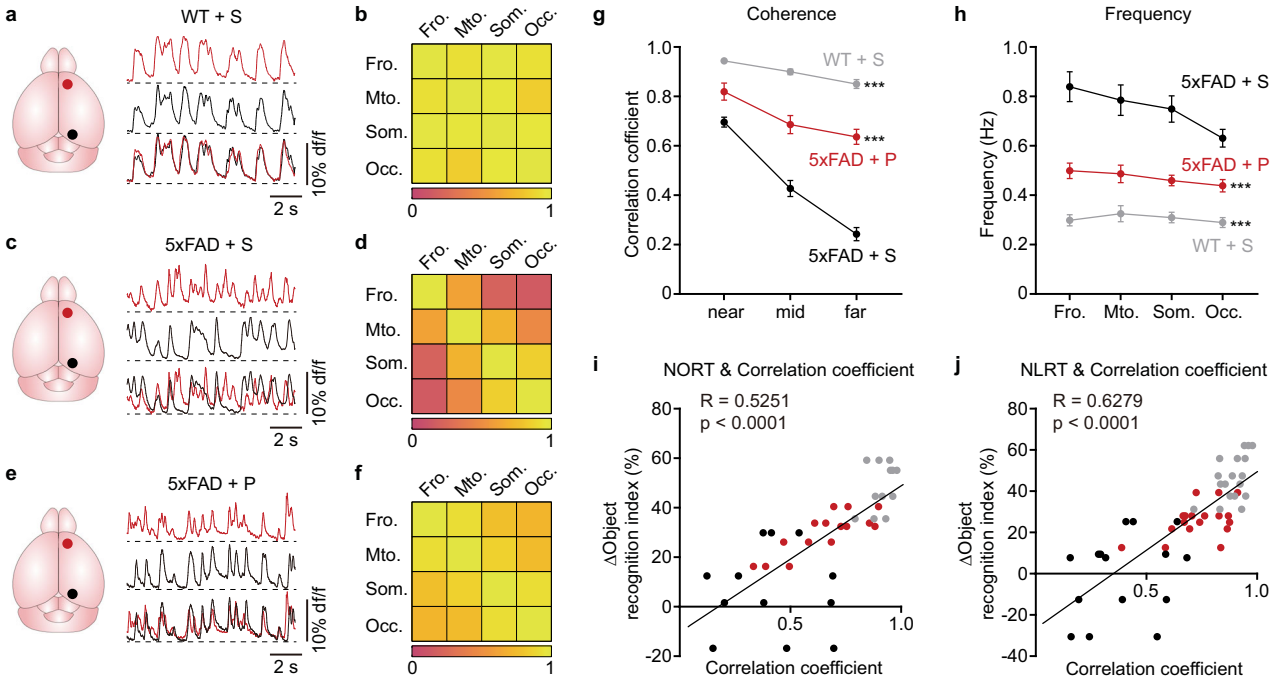

Fig. 2 Pitolisant rescues impaired slow waves in 5xFAD mice. a Representative traces from frontal (red) and occipital (black) cortex of a WT mouse illustrating the normal coherence of slow waves. Traces are superimposed below. **b** Cross-correlation matrix calculated from the same animal shown in a. Rows and columns are labeled by cortical area. **c** Representative traces from frontal (red) and occipital (black) cortex of a 5xFAD mouse with saline illustrating the massive impairment of long-range coherence for slow waves. Traces are superimposed below. **d** Cross-correlation matrix calculated from the same animal shown in c. **e** Representative traces from frontal (red) and occipital (black) cortex of a 5xFAD mouse with pitolisant treatment illustrating the recovery of long-range coherence for slow waves. Traces are superimposed below. **f** Cross-correlation matrix calculated from the same animal shown in e. **g** Summary graph displaying the average cross-correlation coefficients and standard errors plotted against the cortical distance (categorized as near for two neighboring cortical domains, mid for domain pairs separated by one region, and far for domain pairs separated by two regions) in all groups (n = 11 WT mice with saline; n = 12 5xFAD mice with saline; n = 12 5xFAD mice with 20 mg/kg pitolisant; two-way ANOVA with Tukey's multiple comparisons test; WT + S versus 5xFAD + S, $P < 0.0001$; WT + S versus 5xFAD + P, $P < 0.0001$; 5xFAD + S versus 5xFAD + P, $P < 0.0001$). **h** Summary graph of the mean frequencies of slow waves in cortical areas (occ., occipital; som., somatosensory; mot., motor; fro., frontal cortex) in all groups (n = 11 WT mice with saline; n = 12 5xFAD mice with saline; n = 12 5xFAD mice with 20 mg/kg pitolisant; two-way ANOVA with Tukey's multiple comparisons test; WT + S versus 5xFAD + S, $P < 0.0001$; WT + S versus 5xFAD + P, $P < 0.0001$; 5xFAD + S versus 5xFAD + P, $P < 0.0001$). **i** ΔObject recognition index from NORT test plotted against the correlation coefficient (c.c.) in WT + S (grey point, n = 12), 5xFAD + S (black point, n = 12), and 5xFAD + P (20 mg/kg) (red point, n = 15) (spearman correlation with simple linear regression, $P < 0.0001$, R = 0.5251). **j** ΔObject recognition index from NLRT test plotted against the correlation coefficient (c.c.) in WT + S (grey point, n = 18), 5xFAD + S (black point, n = 15), and 5xFAD + P (20 mg/kg) (red point, n = 18) (spearman correlation with simple linear regression, $P < 0.0001$, R = 0.6279). Error bars represent mean ± SEM. $^{*}P < 0.05$, $^{**}P < 0.01$, $^{***}P < 0.001$, ns = no significance.

learned to find the submerged platform. Both the pitolisant- and vehicle-treated male 5xFAD groups spent more time and traveled a longer distance in finding the platform than the WT vehicle group (Fig. 3b; Supplementary Figure 5a, c). Similarly, subsequent probe tests showed that the WT saline group exhibited significantly longer time in the target quadrant than either 5xFAD group, in which these two 5xFAD groups had no significant difference (Fig. 3c; Supplementary Figure 5d).

We then tested whether mice could find the platform in a novel location after the initial learning test (reversal test) (Fig. 3d). We found that the WT vehicle mice found the new platform location more quickly than 5xFAD groups (Fig. 3d; Supplementary Figure 5b, c). Moreover, the pitolisant-treated mice could find the novel location significantly faster than the saline-treated 5xFAD mice (Fig. 3d; Supplementary Figure 5b, c). Probe experiments quantifying time spent in the platform area further illustrated that the pitolisant-treated 5xFAD mice spent significantly more time in the new platform area than the corresponding vehicle controls (Fig. 3e; Supplementary Figure 5d). These results suggest that pitolisant enhances spatial cognitive flexibility in the AD model mice. Additionally, a comparison of swimming speeds showed no significant differences among any of the tested groups during the initial learning (Supplementary Figure 6a) or reversal platform location test (Supplementary Figure 6b), indicating that pitolisant does not affect motor ability in these tests.

Pitolisant reduces Aβ deposition in 5xFAD mice

Due to the known influence of amyloid-beta (Aβ) on slow waves [11], we analyzed the levels of soluble and insoluble Aβ in the cortex of male 5xFAD mice by the enzyme-linked immunosorbent assay (ELISA). We observed that mice treated with pitolisant for 15 days showed lower levels of both soluble Aβ40 (Fig. 4a left) and Aβ42 (Fig. 4b left) in tris buffered saline (TBS) than saline-treated 5xFAD control mice. Similarly, the pitolisant treatment group exhibited lower levels of insoluble Aβ40 (Fig. 4a mid) and Aβ42 (Fig. 4b mid) in sodium dodecyl sulfate (SDS). We noted no significant difference in plasma levels of either Aβ40 (Fig. 4a right) or Aβ42 (Fig. 4b right), indicating that pitolisant does not affect the efflux of Aβ from the brain. Additionally, we found that neither soluble nor insoluble Aβ was detected in the brains or plasma in WT mice (Fig. 4a, b).

As Aβ plaques are classical pathological signs of AD observed in both patients [33] and mouse models [25], we examined Aβ deposition using thioflavin staining in brain slices of 5xFAD mice (Fig. 4c). We found that 5xFAD mice treated with pitolisant for 15 days had significantly decreased Aβ plaque areas in both the

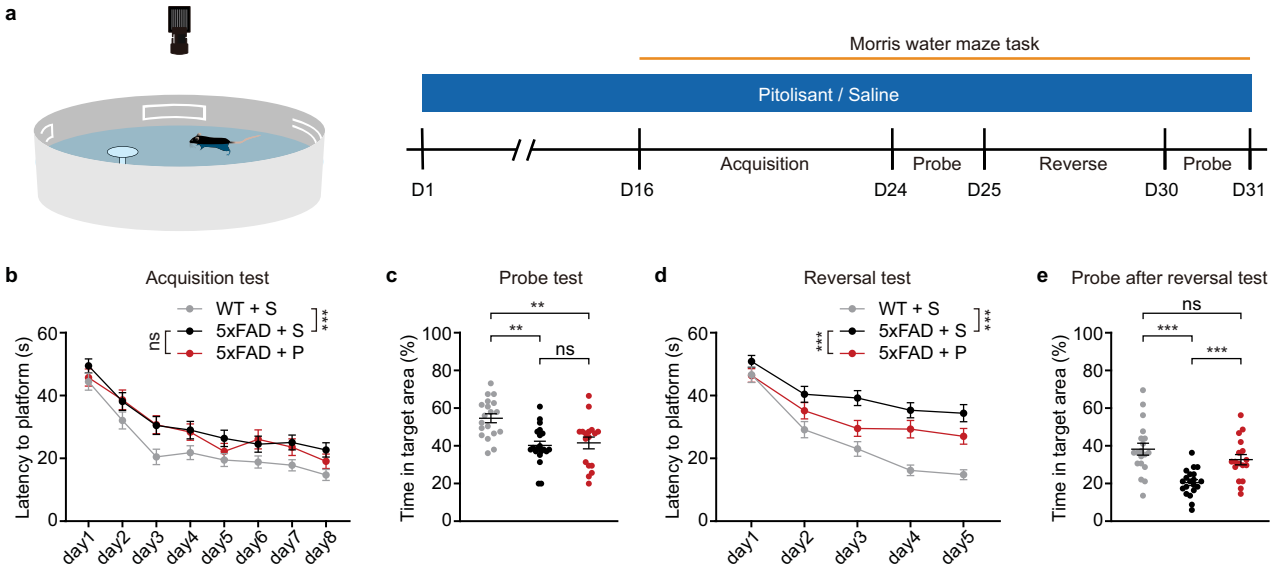

Fig. 3 Pitolisant significantly improves cognitive flexibility in 5xFAD mice. a Left: schematic of the Morris water maze. Right: experimental procedure of the Morris water maze test for 5xFAD mice that either received or did not receive pitolisant (20 mg/kg per day; male mice 6 to 7 months of age). Acquisition tests were performed 3 times per day for 8 days. The reversal test was performed 3 times per day for 5 consecutive days. The probe tests were conducted after the acquisition test and reversal test, respectively. **b** Summary graph showing the latency to find the hidden platform in the acquisition test (n = 19 WT mice with saline, n = 20 5xFAD mice with saline, n = 17 5xFAD mice with 20 mg/kg pitolisant; two-way ANOVA with Tukey's multiple comparisons test; WT versus 5xFAD + S, $P < 0.0001$; 5xFAD + S versus 5xFAD + P, $P = 0.5058$). **c** Time spent in target quadrant area during the probe test after the acquisition test (n = 19 WT mice with saline, n = 20 5xFAD mice with saline, n = 17 5xFAD mice with 20 mg/kg pitolisant; one-way ANOVA with Tukey's multiple comparisons test; WT + S versus 5xFAD + S, $P = 0.0005$; 5xFAD + S versus 5xFAD + P, $P = 0.9285$; WT + S versus 5xFAD + P, $P = 0.0025$). **d** Histogram showing the latency to find the hidden platform in the reversal test (n = 19 WT mice with saline, n = 20 5xFAD mice with saline, n = 17 5xFAD mice with 20 mg/kg pitolisant; two-way ANOVA with Tukey's multiple comparisons test; WT + S versus 5xFAD + S, $P < 0.0001$; 5xFAD + S versus 5xFAD + P, $P < 0.0001$; WT + S versus 5xFAD + P, $P < 0.0001$). **e** Time spent in target quadrant area during the probe test after the reversal test (n = 19 in WT mice with saline, n = 20 5xFAD mice with saline, n = 17 5xFAD mice with 20 mg/kg pitolisant; one-way ANOVA with Tukey's multiple comparisons test; WT + S versus 5xFAD + S, $P < 0.0001$; 5xFAD + S versus 5xFAD + P, $P = 0.0042$; WT + S versus 5xFAD + P, $P = 0.2888$). Each dot represents an individual animal. Error bars represent mean ± SEM. *$P < 0.05$, **$P < 0.01$, ***$P < 0.001$, ns = no significance.

cortex and hippocampus compared to the 5xFAD vehicle group (Fig. 4e). We also quantified Aβ plaques by immunofluorescent staining with the well-characterized 6E10 antibody [34] (Fig. 4d). In line with our above results, pitolisant treatment resulted in a reduced deposition of 6E10-labeled Aβ plaques in the cortex and hippocampus in 5xFAD mice compared to that in the 5xFAD vehicle group (Fig. 4f). We also examined Aβ plaques in the brains of WT mice using thioflavin staining and 6e10 immunofluorescence, and found no detectable Aβ deposition in the brains of WT mice (Fig. 4c–f).

Pitolisant ameliorates dystrophic neurites and enhances lysosomal activity in 5xFAD mice

Dystrophic neurites, i.e., "swollen axons," are commonly found surrounding Aβ deposits, and widespread in the AD brain [35], suggesting substantial impacts on axons and downstream neurons that could, in turn, alter the occurrence and propagation of cortical network activities. We therefore sought to measure the size of dystrophic neurites by immunofluorescent staining for the selective marker of lysosomal components, LAMP1 (lysosomal associated membrane protein 1; Fig. 5a) [35, 36]. We found that male 5xFAD mice treated for 15 days with pitolisant had a reduced proportion of LAMP1-positive regions around plaques, and a lower density of LAMP1-positive clusters in cortex (Fig. 5b). These results suggest the possibility that pitolisant beneficially influences slow-wave activities in 5xFAD mice by alleviating dystrophic neurites and Aβ deposition, and consequently improves cognitive abilities. Furthermore, we did not observe any dystrophic neurites in the brains of WT mice (Fig. 5b).

Impaired lysosomal acidification in neurons has been reported as a pathological feature of AD [37] that leads to the accumulation of immature lysosomes enriched in Aβ in axons and, ultimately, the formation of dystrophic neurites [38]. Additionally, Aβ plaque deposition can deleteriously affect nearby axons, leading to dystrophic neurite development [36]. We therefore examined cathepsin (a type of protease found in lysosomes, primarily responsible for breaking down proteins under optimal pH conditions [37]) levels within dystrophic neurites by immunofluorescent staining. We found that 5xFAD mice treated with pitolisant for 15 days had significantly increased cathepsin B (Fig. 5c) and cathepsin D (Fig. 5d) levels in dystrophic neurites compared with the saline control group.

Previous studies have indicated that neurons expressing H3Rs also co-expressed glutamate decarboxylase or vesicular glutamate transporter [39, 40], suggesting that pitolisant may target both excitatory and inhibitory neurons. To investigate whether pitolisant would affect dystrophic neurites in excitatory or inhibitory neurons, we labeled glutamatergic or GABAergic neurons through viral injections of mCaMK2α-EGFP or mDlx-GFP into the subarachnoid space of 5xFAD mice, respectively, followed by pitolisant or saline administration (Supplementary Figure 7a). Congo red was used to stain plaques. The analysis of neurites near plaques revealed that pitolisant-treated mice had smaller dystrophic neurites in both glutamatergic (Supplementary Figure 7b–d) and GABAergic neurons (Supplementary Figure 7e–g), supporting the pitolisant's effect on improving dystrophic neurites of both excitatory and inhibitory neurons.

In addition, we also examined the enzyme activity of cathepsin B/D in brain homogenates and found that the activity of cathepsin B and D in WT mice was significantly higher than in the 5xFAD group, and pitolisant treatment significantly increased the activity of cathepsin B (Fig. 5e) and cathepsin D (Fig. 5f) in 5xFAD mice,

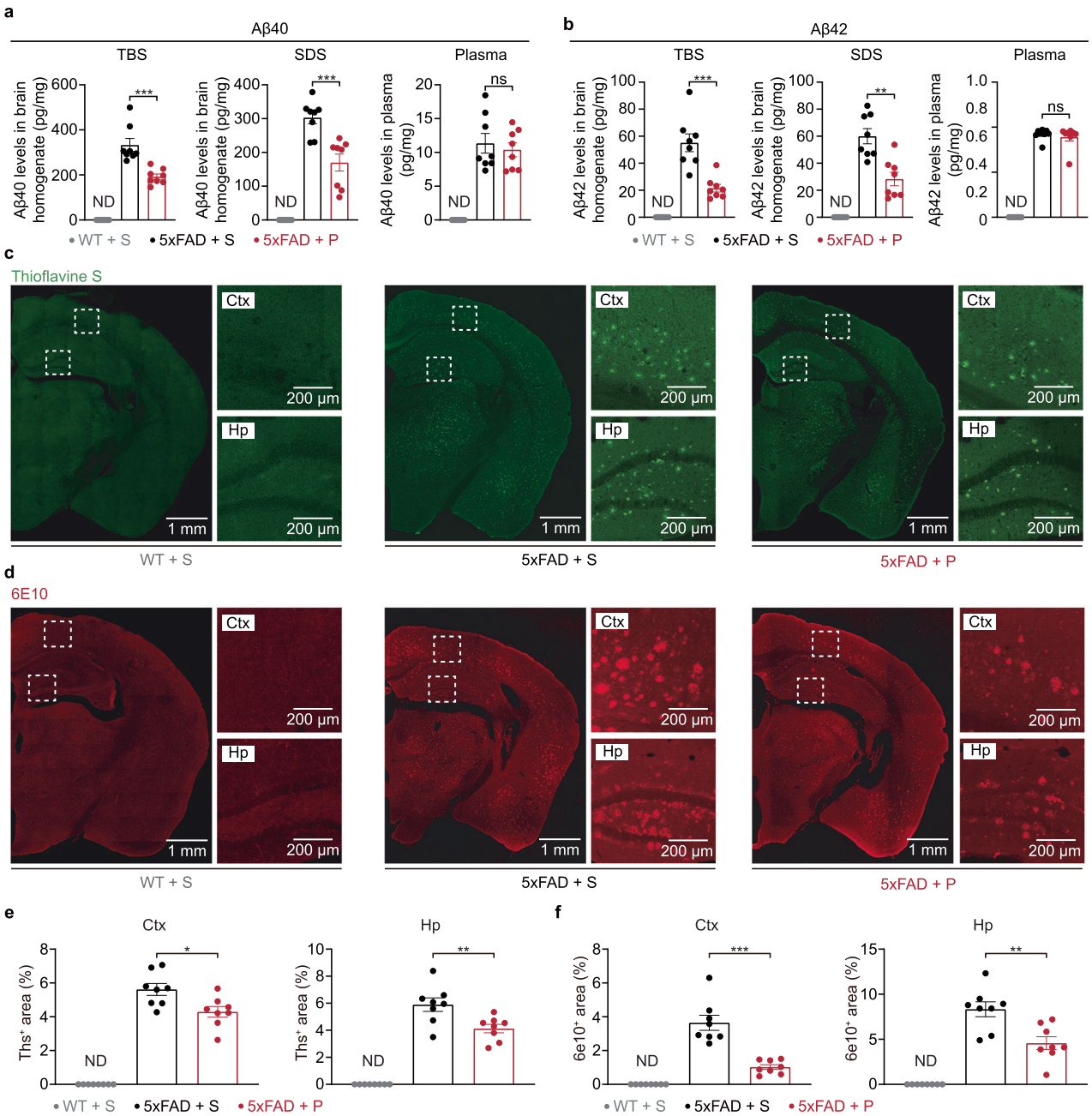

Fig. 4 Pitolisant alleviates Aβ burden in 5xFAD mice. a Left: Levels of soluble Aβ40 in brain homogenate of 5xFAD mice measured by ELISA (n = 8 mice for WT + S; n = 8 mice for 5xFAD + S; n = 8 mice for 5xFAD + P; Mann Whitney test, $P = 0.0002$). Middle: Levels of insoluble Aβ40 in brain homogenate of 5xFAD mice measured by ELISA (n = 8 mice for WT + S; n = 8 mice for 5xFAD + S; n = 8 mice for 5xFAD + P; two-tailed unpaired t test, $P = 0.0007$). Right: Levels of soluble Aβ40 in plasma of 5xFAD mice measured by ELISA (n = 8 mice for WT + S; n = 8 mice for 5xFAD + S; n = 8 mice for 5xFAD + P; two-tailed unpaired t test, $P = 0.6006$). ND = not detected. **b** Left: Levels of soluble Aβ42 in brain homogenate of 5xFAD mice measured by ELISA (n = 8 mice for WT + S; n = 8 mice for 5xFAD + S; n = 8 mice for 5xFAD + P; Mann Whitney test, $P = 0.0003$). Middle: Levels of insoluble Aβ40 in brain homogenate of 5xFAD mice measured by ELISA (n = 8 mice for WT + S; n = 8 mice for 5xFAD + S; n = 8 mice for 5xFAD + P; two-tailed unpaired t test; $P = 0.0009$). Right: Levels of soluble Aβ40 in plasma of 5xFAD mice measured by ELISA (n = 8 mice for WT + S; n = 8 mice for 5xFAD + S; n = 8 mice for 5xFAD + P; Mann Whitney test, P = 0.7984). ND = not detected. **c** Representative images of Aβ (Thioflavin S) staining in the cortex (Ctx) and hippocampus (Hp). **d** Representative images of Aβ (6E10 antibody) staining in the cortex (Ctx) and hippocampus (Hp). **e** Left: quantification of thioflavin S positive area in the cortex (n = 8 mice for WT + S; n = 8 mice for 5xFAD + S; n = 8 mice for 5xFAD + P; two-tailed unpaired t test, $P = 0.014$). Right: quantification of thioflavin S positive area in the hippocampus (n = 8 mice for WT + S; n = 8 mice for 5xFAD + S; n = 8 mice for 5xFAD + P; two-tailed unpaired t test, $P = 0.0097$). ND = not detected. **f** Left: quantification of 6E10 positive area in the cortex (n = 8 mice for WT + S; n = 8 mice for 5xFAD + S; n = 8 mice for 5xFAD + P; Mann Whitney test, $P = 0.0002$). Right: quantification of 6E10 positive area in the hippocampus (n = 8 mice for WT + S; n = 8 mice for 5xFAD+S; n = 8 mice for 5xFAD + P; two-tailed unpaired t test, P = 0.0039). ND = not detected. Each dot represents an individual animal. Error bars represent mean ± SEM. *$P < 0.05$, **$P < 0.01$, ***$P < 0.001$, ns = no significance.

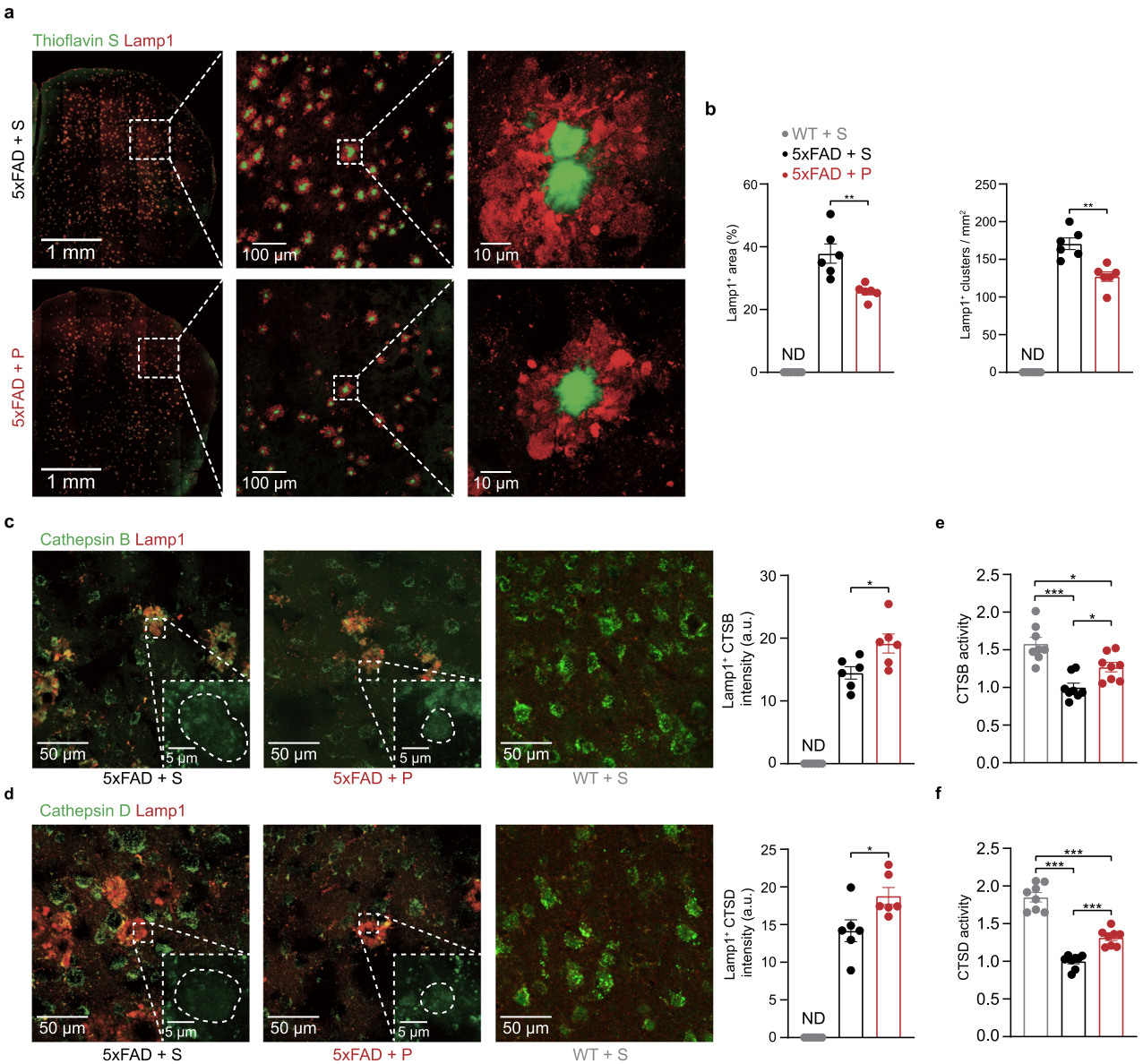

Fig. 5 Pitolisant decreases dystrophic neurites and improves lysosome function. a Representative images of dystrophic neurites (Lamp1 positive staining) around the plaque in 5xFAD with saline or with pitolisant treatment. There are no dystrophic neurites or Aβ plaques in the brains of WT mice. **b** Left: Statistic plot showing lamp1 positive fraction around the plaque in 5xFAD with saline or with pitolisant (n = 6 mice for WT + S; n = 6 mice for 5xFAD + S; n = 6 mice for 5xFAD + P; Mann Whitney test, $P = 0.0022$). Right: Statistic plot showing lamp1 positive clusters count in 5xFAD with saline or with pitolisant (n = 6 mice for WT + S; n = 6 mice for 5xFAD + S; n = 6 mice for 5xFAD + P; Mann Whitney test, $P = 0.0022$). ND = not detected. **c** Left: Double immunofluorescence staining images of cathepsin B (green) and lamp1 (red). Right: Statistic plot showing cathepsin B intensity in lamp1$^+$ area (n = 6 mice for WT + S; n = 6 mice for 5xFAD + S; n = 6 mice for 5xFAD + P; Mann Whitney test, $P = 0.0411$). CTSB = cathepsin B. ND = not detected. **d** Left: Double immunofluorescence staining images of cathepsin D (green) and lamp1 (red). Right: Statistic plot showing cathepsin D intensity in lamp1$^+$ area (n = 6 mice for WT + S; n = 6 mice for 5xFAD + S; n = 6 mice for 5xFAD + P; Mann Whitney test, $P = 0.026$). CTSD = cathepsin D. ND = not detected. **e** Cathepsin B activity in brain homogenate detected by ELISA (n = 8 mice for WT + S; n = 8 mice for 5xFAD + S; n = 8 mice for 5xFAD + P; ordinary one-way ANOVA). **f** Cathepsin D activity in brain homogenate detected by ELISA (n = 8 mice for WT + S; n = 8 mice for 5xFAD + S; n = 8 mice for 5xFAD + P; ordinary one-way ANOVA). Each dot represents an individual animal. Error bars represent mean ± SEM. *$P < 0.05$, **$P < 0.01$, ***$P < 0.001$, ns = no significance.

indicating that pitolisant promotes lysosomal function in the brain.

Are similar effects by pitolisant observed in female 5xFAD mice? To answer this question, we examined whether the pitolisant's effects on AD could be replicated in 6–7-month-old female 5xFAD mice (Supplementary Figure 8a). Immunohistology results showed that 15-day pitolisant treatment (20 mg/kg/d) reduced thioflavin-positive plaques in the cortex and hippocampus, as well as the area and density of dystrophic neurites (Supplementary Figure 8b–e). Wide-field calcium imaging results showed that the slow-wave coherence was enhanced and the frequency was reduced, suggesting the impaired cortical network function was restored (Supplementary Figure 8f–i). Cognitive improvement was observed in both 10-minute and 24-hour delay NORT and NLRT paradigms, with increased interaction times with novel objects or novel location, respectively (Supplementary Figures 8j, 9a–f). Pitolisant also significantly increased cathepsin B/D activity and promoted lysosomal function (Supplementary Figure 8k–l). These experiments reproduced the effect of pitolisant in female 5xFAD mice.

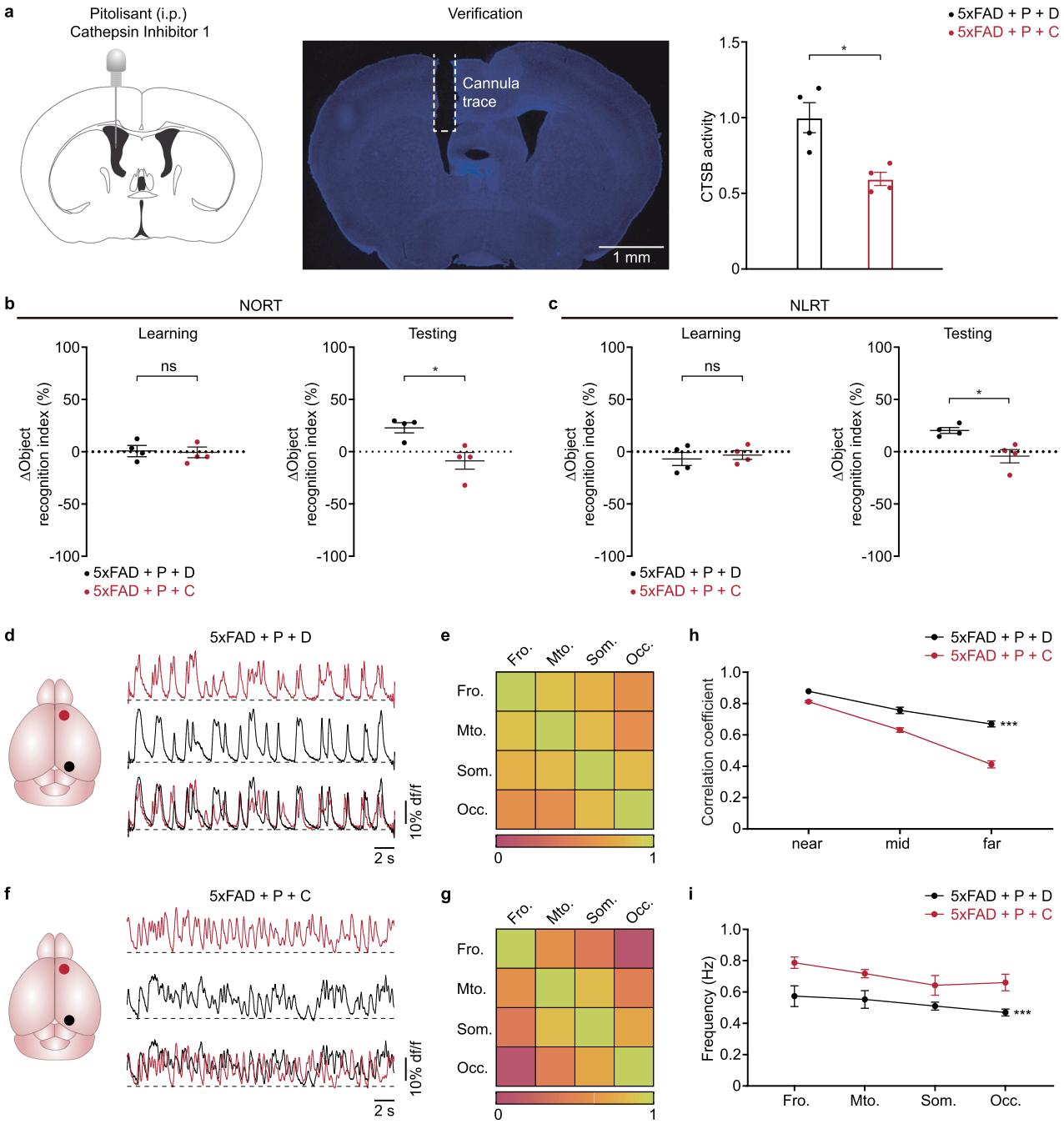

The effects of pitolisant are reversed by inhibiting lysosomal activity in the brain

To investigate whether the enhanced lysosomal function by pitolisant was necessary for its effects in AD mice, we applied cathepsin inhibitor 1 (15 μg in 1 μL) or a dimethyl sulfoxide (DMSO, 1 μL) as control by intracerebroventricular (i.c.v.) infusion via cannula implanted in the lateral ventricle (Fig. 6a left, mid) to inhibit lysosomal function in pitolisant-treated male 5xFAD mice (Fig. 6a right). After confirming that cathepsin inhibitor 1 indeed inhibited cathepsin B activity in brain homogenates (Fig. 6a right), we conducted NORT (Fig. 6b) and NLRT (Fig. 6c) assays, which showed that the positive behavioral effects of pitolisant were significantly reversed by inhibiting lysosomal function. Subsequent wide-field Ca^{2+} imaging showed the cortical slow-wave frequency was higher in the group treated with cathepsin inhibitor 1 than the vehicle control (Fig. 6d, f), while the synchronization of slow-wave activity across cortical regions was lower in the cathepsin inhibitor 1 group than the vehicle control group in 5xFAD mice (Fig. 6e, g). Statistical analysis of slow waves confirmed that inhibition of lysosome function by cathepsin inhibitor 1 significantly reversed the enhanced synchrony (Fig. 6h) and reduced frequency (Fig. 6i) observed in pitolisant-treated AD model mice. The observed differences cannot be explained by cannulation implantation, as we performed wide-field calcium imaging with and without cannulation in WT mice (Supplementary Figure 10a, b). The calcium imaging statistics showed that cannulation did not affect the coherence or frequency of slow waves across cortical regions (Supplementary Figure 10c, d). Additionally, we conducted control experiments using cathepsin inhibitor 1 in WT mice (Supplementary Figure 11a). Similar to the

Fig. 6 Inhibition of lysosomal function impairs the memory-improving effects and ameliorative effect on impaired slow waves of pitolisant in 5xFAD mice. a Left: Schematic of the cannula implantation in the lateral ventricle for pharmacologic administration. Middle: Representative image of cannula position in the lateral ventricle. Right: Quantification of cathepsin B (CTSB) activity in the brain homogenate by enzyme activity assay (n = 4 mice for 5xFAD + P + D; n = 4 mice for 5xFAD + P + C; Mann Whitney test, $P = 0.0286$). P = pitolisant (i.p.), D = DMSO (i.c.v. with cannula), C = cathepsin inhibitor 1 (i.c.v. with cannula). **b** Left: Statistic plot of the NORT learning phase (n = 4 mice for 5xFAD with pitolisant and DMSO; n = 4 mice for 5xFAD with 20 mg/kg pitolisant and cathepsin inhibitor 1; Mann Whitney test, $P = 0.4857$). Right: Statistic plot of the NORT testing phase (n = 4 mice for 5xFAD with pitolisant and DMSO; n = 4 mice for 5xFAD with 20 mg/kg pitolisant and cathepsin inhibitor 1; Mann Whitney test, $P = 0.0286$). **c** Left: Statistic plot of the NLRT learning phase (n = 4 mice for 5xFAD with pitolisant and DMSO; n = 4 mice for 5xFAD with 20 mg/kg pitolisant and cathepsin inhibitor 1; Mann Whitney test, $P = 0.6857$). Right: Statistic plot of the NLRT testing phase (n = 4 mice for 5xFAD with pitolisant and DMSO; n = 4 mice for 5xFAD with 20 mg/kg pitolisant and cathepsin inhibitor 1; Mann Whitney test, $P = 0.0286$). **d** Activity traces from a 5xFAD mouse treated with pitolisant and DMSO. **e** Cross-correlation matrix calculated from the same animal shown in d. **f** Activity traces from a 5xFAD mouse treated with pitolisant and cathepsin inhibitor 1. **g** Cross-correlation matrix calculated from the same animal shown in f. **h** Summary graph displaying the average cross-correlation coefficients and standard errors plotted against the cortical distance (categorized as near for two neighboring cortical domains, mid for domain pairs separated by one region, and far for domain pairs separated by two regions) in all groups (n = 4 mice for 5xFAD with pitolisant and DMSO; n = 4 mice for 5xFAD with 20 mg/kg pitolisant and cathepsin inhibitor 1; two-way ANOVA with Šídák's multiple comparisons test, main effect of manipulation, $P < 0.0001$). **i** Summary graph of the mean frequencies of slow waves in cortical areas for all groups (n = 4 mice for 5xFAD with pitolisant and DMSO; n = 4 mice for 5xFAD with 20 mg/kg pitolisant and cathepsin inhibitor 1; two-way ANOVA with Šídák's multiple comparisons test, main effect of manipulation, $P < 0.0001$). Each dot represents an individual animal. Error bars represent mean ± SEM. $^{*}P < 0.05$, $^{**}P < 0.01$, $^{***}P < 0.001$, ns = no significance.

results before, administration was performed via cannula into the lateral ventricle (Supplementary Figure 11b). The cathepsin B enzyme activity assay results indicated that the WT mice receiving cathepsin inhibitor 1 showed a lower CTSB enzyme activity in the ventricles than the control group, confirming the efficacy of the cathepsin inhibitor 1. In the wide-field calcium imaging results (Supplementary Figure 11d, e), there were no significant differences in slow-wave synchrony and calcium signal frequency between WT mice treated with cathepsin inhibitor 1 and the control group (Supplementary Figure 11f, g). Furthermore, we performed NORT and NLRT behavioral tests, which showed no differences in the interaction time index with the new object or the object moved to a new location between WT mice treated with cathepsin inhibitor 1 and the control group (Supplementary Figure 11h, i). These data suggest that cathepsin inhibitor 1 does not affect neural network activity and cognitive function under physiological conditions.

Overall, the data suggest that pitolisant improves cognitive and pathological abnormalities in AD mice possibly by enhancing neuronal lysosomal function, and that inhibition of lysosomal function can block the pitolisant's effect. To test whether lysosomal inhibition would worsen cognitive deficits and AD pathology, we first chose 3–4-month-old 5xAD mice to avoid "the floor effect". We used cathepsin inhibitor 1 in these mice (Supplementary Figure 12a, b). CTSB enzyme assays confirmed an effective inhibition (Supplementary Figure 12c), and immunofluorescence showed an increase in sulfur-positive plaques, LAMP1-positive neurite area, and aggregate density (Supplementary Figure 12d–j). Wide-field calcium imaging indicated a reduced cortical coherence and an increased calcium signal frequency in treated mice (Supplementary Figure 12k–n), while NORT results showed a decreased interaction with novel objects (Supplementary Figure 12o). These results indicate that lysosomal inhibition accelerates pathology, network dysfunction, and cognitive deficits in early AD mice, which are consistent with the previous studies [41, 42].

Our in vivo results indicate that pitolisant improves cognitive function in the AD mouse model by enhancing neuronal lysosomal function. However, how does pitolisant improve the impaired neuronal lysosomal function? To address this question, we designed in vitro neuronal experiments. First, we confirmed the expression of H3Rs in the mouse neuronal cell line HT22 (Supplementary Figure 13a), consistent with the previous report [43]. Next, we performed a CCK8 cell viability assay to assess the effect of different concentrations of pitolisant incubated for 48 h on cell viability. The results showed that high concentrations of pitolisant (150, 175, 200 μM) were detrimental to the cells, so we chose a concentration of 100 μM for subsequent experiments.

H3R is a GPCR that binds to Gi/o proteins, whose activation inhibits AC and reduces cAMP synthesis [44]. After incubating with 100 nM oligo-Aβ42 for 48 h, ELISA revealed that Aβ significantly lowered cAMP level in neurons, while pitolisant reversed this effect (Supplementary Figure 13c). As cAMP can regulate lysosomal acidification pathways [45], we used a lysosensor probe to assess acidity in neurons (Supplementary Figure 13d). Aβ reduced lysosomal acidity, while pitolisant restored it. The v-ATPase inhibitor BafA1 served as a positive control, showing the lowest acidity. PKA inhibitor H-89 blocked pitolisant's effect (Supplementary Figure 13e). Furthermore, CTSB enzyme activity assays confirmed pitolisant's effects in vitro (Supplementary Figure 13f). These results suggest pitolisant modulates lysosomal acidity via the H3R/cAMP/PKA pathway.

DISCUSSION

In this study, we reveal that pitolisant, a previously approved first-line drug to treat narcolepsy [46], can restore disrupted cortical slow waves and cognitive deficits in the 5xFAD mouse model via a mechanism of promoting lysosomal function. Up-regulating lysosomal function is known to enhance the overall clearance rate of toxic substances [47, 48], such as the soluble Aβ as well as all other endogenous toxins in the brain that have been identified as vicious players in the pathogenesis of AD [49–53], thereby resulting in a brain-wide synergistic effect of rescuing neuronal dysfunctions and cognitive dysfunctions. Indeed, our data (Fig. 4) show that not only the plaque but also the soluble Aβ were reduced by almost 2-fold in the treatment group. It warrants mention that H_3R, the specific target of pitolisant, is also expressed in microglia [54] and astrocytes [55] that are the main work force of toxic substance clearance in the brain. Therefore, this 'side-effect' of pitolisant to rescue AD in an animal model can be mechanistically interpreted (Fig. 6) as a new, beneficial 'main effect' of enhancing toxin clearance via up-regulating lysosome functionality.

What could be the possible factors involved in disrupting slow-wave activity in AD mice? Dystrophic neurites emerged as a hallmark of AD pathology [35, 38] that may interfere with action potential propagation along axons, resulting in abnormal long-range connectivity among distant brain regions [4, 56], which could contribute to desynchronizing slow waves across cortex-wide networks. Additionally, dystrophic neurites could further impair synaptic plasticity by disrupting the precise timing of synaptic activity between pre- and post-synaptic neurons [57].

Along these lines, we indeed found that the abundance of dystrophic neurites surrounding Aβ plaques was significantly lower after 15-day pitolisant treatment in the AD mouse brain, supporting the notion that dystrophic neurites serve as a structural basis leading to the disruption of neural network function in AD.

Neuronal hyperactivity in early stage of AD was thought to be a key factor affecting slow-wave oscillation. There is a strong correlation between the neuronal hyperactivity and the disturbance of long-range brain circuits in animal models of AD [11]. Neuronal hyperactivity in AD patients is also associated with impaired sleep-associated slow oscillations [58]. Moreover, experimentally restoring slow-wave oscillation can rescue cognitive deficits in AD mouse models [11]. The presence of soluble Aβ has been suggested to interfere with synaptic transmission between neurons [59], which could also disrupt the balance between excitatory and inhibitory neurons, thus resulting in abnormal neuronal network activity. Consistent with this, we found that soluble Aβ in brain homogenates was significantly reduced after 15 days of pitolisant treatment (Fig. 4a, b).

In 5xFAD mice, overexpression of mutant human amyloid precursor protein (APP) and presenilin 1 (PSEN1) leads to heavy Aβ accumulation in poorly acidified autophagic lysosomes, resulting in the formation of Aβ plaques [37]. Consequently, Aβ oligomers near these plaques can enter surrounding axons, inducing the formation of numerous dystrophic neurites that are also enriched with such poorly acidified lysosomes [36], further inhibiting neuronal network function. Therefore, dysregulation of lysosomal acidification is possibly a critical factor in the development and progression of plaques and dystrophic neurites. Consistent with this hypothesis, we found that the plaque burden and soluble Aβ levels were both decreased in AD mice treated with pitolisant. In addition, cathepsin content in dystrophic neurites and cathepsin activity (cathepsin B and cathepsin D) in brain homogenates were both increased after pitolisant treatment, suggesting improved lysosomal function. Importantly, inhibiting lysosomal function in vivo by injection of cathepsin inhibitor 1 significantly reversed the therapeutic effects of pitolisant on improving memory performance and restoring slow-wave activity, further illustrating that improved lysosomal function in neurons underpins the anti-AD mechanism of pitolisant.

As a presynaptic autoreceptor, H_3R regulates histamine synthesis and release through negative feedback mechanisms [60]. It is known that H_3R antagonists can elevate brain histamine levels via the release from the tuberomammillary nucleus (TMN) neurons [60, 61]. However, as a presynaptic heteroreceptor, H_3R also negatively modulates the release of other neurotransmitters [44]. Furthermore, H_3R has been detected in postsynaptic neurons, where it regulates the activity of cholinergic neurons [62]. Given the fact that acute administration of pitolisant has no effects on neuronal network function and behavior, we propose the therapeutic mechanism of pitolisant is not mediated by its direct influence on neuronal activity.

Cognitive flexibility of spatial memory involves two key processes, the formation of new memories and the weakening or extinction of old memories, both of which are impaired in AD [59]. The pitolisant-treated AD mice showed no difference in the initial learning to navigate a location but performed better in the reversal learning compared to untreated mice. This result suggests the pitolisant improves cognitive flexibility without changes in the initial acquisition task. This also indicates that acquisition and reversal learning may involve different neural circuits or cellular mechanisms. Further studies are required to dissect the neural mechanisms underlying cognitive flexibility.

We have preliminarily explored the molecular mechanism by which pitolisant improves neuronal lysosomal function. As a GPCR coupled with Gi/o protein, H3R inhibits adenylate cyclase, thereby reducing cAMP levels [44]. Consistent with this, we found that pitolisant could increase the low cAMP levels caused by Aβ incubation. Lysosomal acidification is primarily maintained by the vacuolar ATPase (v-ATPase), a multimeric enzyme complex that pumps protons from the cytosol into the lysosomal lumen [63], and the activation of this complex requires PKA [64]. In line with this, we found that pitolisant alleviates the abnormal lysosomal acidity caused by Aβ incubation, while the competitive inhibitor H89, which prevents cAMP from binding to PKA, abolishes pitolisant's ability to improve the lysosomal acidity and cathepsin dysfunction induced by Aβ. Therefore, pitolisant may enhance lysosomal function by ameliorating neuronal lysosomal acidification dysfunction through the H3R/cAMP/PKA axis.

In 5xFAD mice, Aβ accumulates in the acidic dysfunctional lysosomes of neurons, leading to cell death [37]. In this study, we found that pitolisant enhances lysosomal function by promoting lysosomal acidification. Therefore, we speculate that the reduction of soluble Aβ in brain homogenates after 15 days of pitolisant treatment may be related to the enhanced lysosomal function in neurons. Consistent with this, another H3R antagonist (thioperamide) has been found to rescue neuronal loss in APP/PS1 mice [65]. Therefore, enhancing lysosomal acidification in neurons may be one of the mechanisms underlying the neuroprotective effects of pitolisant.

In addition to neuronal mechanisms, the neuroglial microenvironment plays a crucial role in preventing the formation of dystrophic neurites around plaques [36]. H3R is expressed in both microglia and astrocytes [66]. Although previous studies have showed that microglia do not respond to H3R-mediated regulation [67], calcium imaging studies have suggested that the phagocytic activity of microglia can be directly controlled by histamine H2 receptor (H2R) and indirectly controlled by purinergic signaling mediated by histamine H1 receptor (H1R) on astrocytes [67]. Further studies are required to explore the interactions between neuronal lysosomal mechanisms and histamine-dependent neuroglial cell mechanisms.

In summary, our results demonstrate that the FDA-approved H_3R antagonist, pitolisant, can improve slow waves and cognitive impairments in 5xFAD mice by enhancing neuronal lysosomal function. Based on the fact that pitolisant has been already approved worldwide for its safety, this animal model study paves the road to launch new clinical trials to systematically test the effect of pitolisant treatment in rescuing AD patients regardless of their disease progression.

MATERIALS AND METHODS

Subject

This study followed the guidelines approved by the Animal Ethics Committee of Guangxi University. We used heterozygous 5xFAD mice (Tg6799, C57BL6), which express mutant human APP and PSEN1 (APP KM670/671NL: Swedish, I716V: Florida, V717I: London, PSEN1 M146L, L286V), along with age-matched wild-type littermate control mice, aged 6 to 7 months, as the animal subjects. The mice were housed in optimouse cages under controlled conditions, with a 12-hour light/dark cycle, and were provided ad libitum access to food and water. If not specifically stated otherwise, male mice were used in the experiments. Pitolisant (#S87162, Yuanye) was dissolved in saline and administered to the animals via intraperitoneal injection (i.p.). Cathepsin inhibitor 1 (#GC16181, GLPBIO) was dissolved in DMSO and administered to the animals via intracerebroventricular injection (i.c.v.).

Stereotaxic surgery for wide-field Ca^{2+} imaging

We induced anesthesia in all mice using a mixture of 3% isoflurane in air. During surgery, we reduced the concentration of isoflurane to 0.8–1%. We maintained a consistent level of anesthesia characterized by the absence of reflexes (such as tail clips) and a respiratory rate of 80–110 breaths per minute. To ensure a stable body temperature of 37 ± 0.5 °C, we placed the mice on a warming plate. We protected the mice's eyes with Bayer's Bepanthen to prevent desiccation. After removing the skin from the skull area, we affixed the recording chamber to the skull using a custom-made

adhesive and light-curing Tetric N-Flow (Lvoclar Vivadent AG). For large-scale Ca^{2+} imaging, we created a cranial window over both cortical hemispheres while ensuring the dura remained intact, taking extreme care not to damage the underlying cortical tissue. For large-scale Ca^{2+} imaging following cannula implantation, we created a cranial window over only half of the cortical hemispheres. The recording chamber was perfused with artificial cerebrospinal fluid (ACSF) containing 125 mM NaCl, 4.5 mM KCl, 26 mM NaHCO3, 1.25 mM NaH2PO4, 2 mM CaCl2, 1 mM MgCl2, 20 mM glucose, and adjusted to a pH of 7.4.

Stereotaxic surgery for cannula implantation

We implanted cannula (RWD Life Science) into the lateral ventricle at the following coordinates relative to bregma: AP: 0.0 mm, ML: 1.0 mm, DV: −2.0 mm. After completing the implantation, we secured the cannula onto the skull surface using light-curing Tetric N-Flow (Lvoclar Vivadent AG) and dental cement. Before conducting wide-field Ca^{2+} imaging, we removed the cannula and sealed the hole using Vetbond Tissue Adhesive (3 M). To confirm the position of the cannula, we conducted brain sectioning following perfusion with 4% PFA at the conclusion of all experiments.

Wide-field Ca^{2+} imaging in vivo

In this investigation, cortical regions were visualized utilizing a standard volume loading technique, and the cortex was stained employing the fluorescent Ca^{2+} indicator Cal 520 AM. Cal 520 AM was solubilized in a 20% Pluronic F-127 dimethyl sulfoxide (DMSO) solution at a concentration of 10 mM, subsequently diluted to a final concentration of 0.5 mM in ACSF. This solution was administered to multiple regions within the exposed cranium utilizing a glass micropipette and an RWD microinjector, with an injection rate of 3 nl/s and a volume of 500 nl per injection site. This method yielded near-complete labeling of the entire cortex. High-speed digital imaging was conducted utilizing a Dhyana 400BSI camera (TUCSEN) in conjunction with a fluorescence microscope and a 2x/0.08 NA apochromat objective (Olympus) or a 2-CAFE imaging system (2-Channel Alternating exposure wide-Field Explorer, NewLight OptoInstrument Co., Ltd; see: www.newlightxhr.com). Images were captured at a frequency of 30 Hz with a resolution of 1024 × 1024 pixels employing the Mosaic v1.4 data acquisition software provided by the manufacturer.

Imaging data analysis

We employed custom software packages, including LabVIEW 2014, Igor Pro 5.0 (Wavemetrics Inc., USA) and MATLAB 2016b (MathWorks, USA), for offline data analysis, ensuring the reliability of our results. The LOTOS program, based on LabVIEW, facilitated the calculation of Ca^{2+} signals for each region of interest (ROI) as relative fluorescence changes ΔF/F = (F-F0)/F0 over time, with F0 estimated as the 25th percentile of fluorescence values for each ROI. Given that heart rate artifacts manifest at frequencies above 4 Hz, falling within the relevant signal range, we employed a custom MATLAB filtering program based on the fast Fourier transform to eliminate cardiac-related artifacts.

To explore the spatial coherence of cortical Ca^{2+} signals, we segmented each hemisphere of the cortex into four regions spanning from anterior to posterior: frontal cortex, motor cortex, somatosensory cortex, and parietal cortex. Coherence assessment was conducted based on the mean Ca^{2+} signal of each cortical region over a 30-second period. Calculation of the frequency of Ca^{2+} transients involved the initial detection of transient peaks. Subsequently, the Ca^{2+} transient data underwent smoothing using a window span of 3, with the first round of transient peaks required to exhibit a minimum peak prominence equivalent to the signal standard deviation. Only one peak per second was permitted in this initial round. Subsequent measurement of transient peaks in the second round was constrained by the average peak width, thereby determining the final peak components.

Behavior assays

The behavior assays took place during the light phase of the diurnal cycle (from 07:00 h to 19:00 h). Mice were randomly assigned to the experimental group and underwent specific behavioral testing. Before commencing the experiments, mice underwent a habituation phase consisting of 1–2 min of researcher manipulation for 7 consecutive days. This procedure occurred in a designated holding room, where each mouse remained for the duration of the manipulation. To minimize stress and familiarize the mice with the testing environment, each mouse was transported from the holding room to the vicinity of the behavioral testing room in its homecage before each experimental session. Throughout all behavioral experiments, blind analysis was employed to mitigate potential observer biases in the experimental group.

Novel object recognition test

We conducted the NORT in an open square arena measuring 40 cm×40 cm x 40 cm. The test comprised three stages: habituation, learning, and testing. Initially, on the first day, the mice were allowed to freely explore the arena for 10 min to acclimate to the environment. The second day was designated as the learning stage, where two identical objects were placed in opposite corners of two quadrants within the arena. The mice were then permitted to explore these objects for 10 min. After this exploration, the mice were promptly returned to their homecage. Ten minutes later, the testing stage commenced, during which one of the objects was substituted with a novel one. The experimental mice were introduced into the arena for a final 10-minute period of free exploration. In this article, there is another version of this paradigm, where the interval between learning and testing is 24 h instead of 10 min.

We recorded the behavior of the mice using a 30 Hz infrared camera (DS-2CD5047EFWD, HIKVISION) with a spatial resolution of 1280 × 720. Throughout both the training and testing stages, a trained analyst, blinded to the experimental groups, manually reviewed the recorded video to assess the time spent exploring each object, as indicated by sniffing behavior. This information facilitated the evaluation of object preference among the mice. The ΔObject recognition index was computed utilizing the subsequent equation:

$$\Delta Object\ recognition\ index = \frac{(T_n - T_f)}{(T_n + T_f)}$$

Novel object location recognition test

Similar to the NORT, we conducted the NLRT in an open square arena measuring 40 cm×40 cm x 40 cm. The task comprised three stages: habituation, learning, and testing. Initially, on day 1, mice were given a 10-minute period of free exploration in the arena to acclimatize. On day 2, designated as the learning stage, two identical objects were randomly positioned in separate quadrants of the arena. Mice were then allowed to explore these objects for 10 min. Subsequent to this exploration, the mice were promptly returned to their homecages. Ten minutes later, the testing stage commenced, during which one of the objects was relocated to a different quadrant, while the other object remained in its original position. The experimental mice were then introduced into the arena for a final 10-minute period of free exploration. In this article, there is another version of this paradigm, where the interval between learning and testing is 24 h instead of 10 min. We recorded the behavior of the mice using a 30 Hz infrared camera (DS-2CD5047EFWD, HIKVISION) with a spatial resolution of 1280 × 720. Throughout both the training and testing stages, a trained analyst, blinded to the experimental group, manually reviewed the recorded video to assess the time spent exploring each object, as indicated by sniffing behavior. This information facilitated the evaluation of location preference among the mice. The ΔObject location recognition index was computed utilizing the subsequent equation:

$$\Delta Object\ location\ recognition\ index = \frac{(T_n - T_f)}{(T_n + T_f)}$$

Morris water maze

We conducted the Morris water maze task in a cylindrical water tank (diameter 150 cm, height 40 cm), where water at a temperature of 20 °C ± 1 °C was rendered opaque by the addition of titanium dioxide. Concealed from view, a platform positioned at the center of one quadrant remained submerged beneath water elevated 1.5 cm above its surface. Multiple visual cues strategically positioned on the pool walls, facilitated spatial orientation for the platform's location.

Mice were introduced to the pool one day prior to the initiation of the Morris water maze task to allow for acclimatization, with non-swimmers excluded from the study. Each day of the acquisition trials entailed three consecutive 60-second trials, during which mice navigated in search of the hidden platform. In instances where the platform remained elusive within

the allocated timeframe, mice were guided to it and given 60 seconds to familiarize themselves with its location before returning to their cages, where the heater was activated. The acquisition phase extended over eight days, culminating in a probe test on the ninth day, during which the platform was removed, and mice underwent a single 60-second trial. Subsequently, commencing on the tenth day, the platform was relocated to the opposite quadrant, initiating three reversal tests daily for five consecutive days. Following the reversal tests, the platform was removed, and a single 60-second probe test was conducted. Throughout all training and testing procedures, video recordings were captured using a 30 Hz infrared camera (DS-2CD5047EFWD, HIKVISION) with a spatial resolution of 1280 ×720. A custom MATLAB program facilitated tracking of the animals' positions and data collection.

Tissue and cell immunofluorescence

For tissue immunofluorescence, we perfused the mice with 4% paraformaldehyde to initiate brain fixation. Subsequently, we collected, fixed, and dehydrated the brains in 4% paraformaldehyde solution supplemented with 15% sucrose. Following dehydration, we sectioned the brains into 50-micrometer slices using a freezing microtome (CryoStar NX50, Thermo Scientific). These slices underwent treatment with PBS-T (PBS with Triton X-100) and donkey serum for 1 h, followed by a 24-hour incubation with primary antibodies at 4 °C. After thorough washing with PBS, the slices were subjected to a 2-hour incubation with secondary antibodies. Preceding their mounting onto microscope slides, the slices underwent three additional washes with PBS.

For immunofluorescence, the HT22 cell line (mouse neuronal cell line) was grown on glass coverslips to 70% confluence. The cell cultures were washed with PBS and fixed with 4% paraformaldehyde for 20 min. After washing with PBS, the cells were permeabilized with 0.3% (v/v) Triton X-100 in PBS for 10 min, rinsed three times in PBS, and treated with 10% (v/v) donkey serum for 1 h. The cells were then incubated overnight at 4 °C with the primary antibody, followed by a 1-hour incubation at room temperature with the secondary antibody, and finally mounted on microscope slides with a drop of mounting medium.

Antibody list

The staining process employed the following primary antibodies: we used mouse monoclonal anti-6e10 (#803015, Biolegend, 1:250), rat monoclonal anti-Lamp1 (#1D4B, DSHB, 1:250), rabbit monoclonal anti-HRH3 (#M06436, Boster, 1:250), rabbit monoclonal anti-cathepsin D (#ab75852, Abcam, 1:250), and rabbit monoclonal anti-cathepsin B (#ab214428, Abcam, 1:250). For secondary antibodies, we utilized donkey polyclonal anti-mouse Alexa Fluor 555 (#ab150106, Abcam, 1:500), donkey polyclonal anti-rat Alexa Fluor 555 (#ab150154, Abcam, 1:500), and donkey polyclonal anti-rabbit Alexa Fluor 488 (#ab150073, Abcam, 1:500).

Thioflavin S staining

We used Thioflavin S staining to label Aβ plaques. In brief, we immersed the brain sections in 0.002% Thioflavin S solution (T1892-25G, Sigma-Aldrich) in 50% ethanol for 10 min, followed by two washes with 50% ethanol and one wash with PBS. Subsequently, we mounted the sections onto glass slides and imaged them using confocal microscopy.

Subarachnoid injection

AAV2/9-mDlx-eGFP-WPRE-pA and AAV2/9-mCaMKIIa-EGFP-WPRE-pA viruses were purchased from Taitool (#S0550-9 and #S0241-9). The virus was injected into the subarachnoid space of one hemisphere of the mouse brain. Briefly, under isoflurane anesthesia, a thin skull window approximately 1 mm in diameter was created using a dental drill at 0.0 mm anterior-posterior and 2.0 mm mediolateral from bregma. A 1 ml syringe needle was used to gently lift the thinned skull to expose the underlying brain tissue, and the dura mater was carefully removed with tweezers to avoid damaging the brain parenchyma. The viral solution was aspirated into a glass electrode pulled with a P1000 (SUTTER), and a silicone tube connected to a 1 ml syringe was fitted onto the glass electrode. The tip of the glass electrode was then inserted into the exposed subarachnoid space, and 5 μl of the viral solution was slowly injected by pushing the syringe. After injection, the glass electrode was removed, and the mouse scalp was sutured. The mouse was placed on a heating pad for recovery. Four weeks after injection, the mice were sacrificed, and brain sections were collected for confocal microscopy image data acquisition.

Congo Red staining

We performed co-labeling experiments using Congo Red (C6767, Sigma-Aldrich) and EGFP virus tags. Briefly, we immersed brain slices in a 0.01% Congo Red solution (75% ethanol) for 10 min, followed by two washes with 50% ethanol and one wash with PBS. Subsequently, we mounted the slices with coverslips and imaged them using a confocal microscope.

Confocal microscopy

Images were acquired using an Olympus FV3000 or Zeiss LSM 900 laser confocal microscope. Laser and detector parameters remained consistent throughout each analysis. For Ths staining and 6E10 immunofluorescence assays, images were captured utilizing an Olympus 20x/0.85 NA oil immersion objective, acquiring images at a resolution of 1024×1024 pixels, employing a 3-slice projection with a z-step size of 2 μm.

To delineate the area occupied by dystrophic neurites proximal to the plaques, images were obtained utilizing an Olympus 60x/1.42 NA oil immersion objective at a 3x magnification, achieving a resolution of 1024 × 1024 pixels, employing a 3-slice projection with a z-step size of 1 μm.

Quantification of dystrophic neurite density was performed using images acquired utilizing an Olympus 20x/0.85 NA oil immersion objective at a 3x magnification, achieving a resolution of 1024 × 1024 pixels, employing a 3-slice projection with a z-step size of 1 μm.

For cathepsin B and cathepsin D immunofluorescence assays, images were captured using an Olympus 60x/1.42 NA oil immersion objective at a 5x magnification, acquiring images at a resolution of 1024 × 1024 pixels, employing a 3-slice projection with a z-step size of 1μm. Subsequent image processing and analysis were conducted using FIJI (ImageJ) software.

For the detection of virus-labeled dystrophic neurites around plaques, images were captured using a 40x/0.95 NA objective at a 2x magnification, with a resolution of 1024 × 1024 pixels. A 4-slice projection was employed with a z-step size of 1 μm. Subsequent image processing and analysis were also performed using FIJI (ImageJ) software.

Aβ and cAMP enzyme-linked immunosorbent assay (ELISA)

The mice designated for ELISA and enzyme activity assays underwent perfusion with PBS only, followed by brain extraction. Brain tissue was pulverized into homogenate using liquid nitrogen in a mortar. The resultant brain homogenate was extracted with 0.1 M Tris-buffered saline (TBS) and centrifuged at 13,000 g for 1 h at 4 °C. The supernatant, obtained post-centrifugation, contained soluble Aβ components. The residual pellet containing insoluble Aβ was then dissolved in 2% sodium dodecyl sulfate buffer (SDS) and subjected to another round of centrifugation at 13,000 g for 1 h at 4 °C. The supernatant from this centrifugation step contained insoluble Aβ components. Commercial ELISA kits (Elabscience, E-EL-M3009 for mouse Aβ40, E-EL-M3010 for mouse Aβ42) were employed to quantify Aβ40 and Aβ42 levels in the brain tissue of 5xFAD mice. ELISA procedures were conducted following the manufacturer's protocols. Subsequently, the data were normalized to total protein content.

For the preparation of cell samples, cells in the culture plate were washed with PBS, and RIPA lysis buffer was added. The mixture was incubated on ice for 30 min to fully release intracellular components. The supernatant was collected by centrifugation at 2000×g for 10 min to obtain the cell lysate. cAMP level in cell lysate was quantified by ELISA according to the manufacturer's protocol (E-EL-0056c, Elabscience).

Enzyme activity assays for cathepsin B and cathepsin D

Enzyme activities from brain homogenate, specifically cathepsin B and cathepsin D, were quantified employing assay kits (ab65300 and ab65302, Abcam) according to the manufacturer's instructions. For the cathepsin D activity assay, fractions were incubated in darkness at 37 °C for 1 h with the cathepsin D substrate GKPILFFRLK (Dnp)-D-R-NH2 labeled with MCA. Fluorescence emission was measured at Ex: 328 nm and Em: 460 nm using a transparent 96-well plate (Costar). In the case of the cathepsin B activity assay, fractions were subjected to a similar incubation condition but with the cathepsin B substrate RR labeled with amino-4-trifluoromethyl coumarin. Fluorescence was detected at Ex: 400 nm and Em: 505 nm using a transparent 96-well plate (Costar). All enzyme activity measurements were conducted employing the SpectraMax M2 Microplate Reader.

HT22 cell culture procedures

HT22 cells (Sunncell) were cultured in DMEM (Sunncell) supplemented with 10% FBS and maintained in a 37 °C, 5% CO2 incubator.

CCK-8 assay

Each 96-well plate was inoculated with cells at a density of 2 × 10^4 cells per well. According to the manufacturer's instructions, cell viability was measured using the Cell Counting Kit 8 (FineTest, #FNCK064). A total of 100 µl of CCK8 working solution was added to each well and incubated in the dark for 1 h. Absorbance at 450 nm was measured using the Epoch Microplate Reader (Agilent). Cell viability was assessed 48 h after treatment with different concentrations of pitolisant.

Oligo-Aβ42 preparation procedures

The preparation method for Oligo-Aβ42 (AS-24224, AnaSpec) is as follows: peptides dissolved in DMSO (5 mM) were diluted to 100 µM with DMEM and sonicated for 10 min. A portion of the peptides was then incubated at 37 °C for 24 h, followed by incubation at 4 °C for 24 h. After that, the solution was centrifuged at 16,000 g for 15 min, and the collected supernatant was used as Oligo-Aβ42.

Lysosensor probing

In the LysoSensor experiments, HT22 cells were stained with LysoSensor Green DND-189 (Yeasen, #40767ES50) according to the manufacturer's protocol. Briefly, HT22 cells were incubated with 1 µM LysoSensor in culture media for 1 h at 37 °C. Subsequently, 100x Hoechst 33342 was added to achieve a final concentration of 1x, and the cells were incubated for 10 min at 37 °C. Images were then acquired using an Axiovert fluorescence microscope (Zeiss).

Statistical analysis

The data analysis was conducted in a blinded fashion to ensure impartiality, with the analyst uninformed of the experimental group allocations. Sample sizes for each group are provided in the corresponding figure legends. The data in the figure are presented as mean ± standard error of the mean (SEM). Prism 9 software was utilized for statistical data analysis.

To assess the impact of different doses of pitolisant on cognitive abilities, we fitted the following equation to the data:

$$Y = a + \frac{b}{1 + 10^{(Logc - X) * d}}$$

To evaluate the relationship between slow-wave activity and cognitive abilities, we fitted the following equation to the data:

$$Y = a * X - b$$

In the statistical tests, D'Agostino-Pearson, Shapiro-Wilk and Kolmogorov-Smirnov test was used to determine whether the data follow a normal distribution. Brown-Forsythe test was used to test the homogeneity of variances between groups.

For the data within each group meets the criteria of normal distribution and equal variance, two-tailed paired and unpaired t-test were employed for comparing two paired and unpaired groups of data. The Mann-Whitney test was applied when the data does not satisfy the assumption of normal distribution.

For comparing more than two groups of data, one-way ANOVA followed by Tukey's multiple comparisons test was applied when the data in each group satisfies the assumptions of normal distribution and homogeneity of variance. When the data in each group meet the assumption of normal distribution but have unequal variances, Brown-Forsythe and Welch ANOVA followed by Dunnett's T3 multiple comparisons test were applied. When the data in each group do not meet the assumption of normal distribution, the Kruskal-Wallis test followed by Dunn's multiple comparisons test was applied.

Two-way ANOVA with Tukey's multiple comparisons test or Šídák's multiple comparisons test was used to compare the effects of two or more numerical variables on the dependent variable.

Statistical significance was set at $\alpha = 0.05$. Symbols denoting significance were employed as follows: (*) for $P < 0.05$, (**) for $P < 0.01$, and (***) for $P < 0.001$. Non-significant results were indicated as $P > 0.05$ (ns).

DATA AVAILABILITY

The data produced and/or scrutinized in this study can be accessed upon request from the corresponding author. As far as we are aware, no datasets were acquired from public repositories, nor were any datasets deposited into such repositories during this investigation.

REFERENCES

1. Scheltens P, De Strooper B, Kivipelto M, Holstege H, Chételat G, Teunissen CE, et al. Alzheimer's disease. Lancet. 2021;397:1577–90. https://doi.org/10.1016/s0140-6736(20)32205-4
2. van Dyck CH, Swanson CJ, Aisen P, Bateman RJ, Chen C, Gee M, et al. Lecanemab in early Alzheimer's disease. N Engl J Med. 2023;388:9–21. https://doi.org/10.1056/NEJMoa2212948
3. Sims JR, Zimmer JA, Evans CD, Lu M, Ardayfio P, Sparks J, et al. Donanemab in early symptomatic Alzheimer disease: the TRAILBLAZER-ALZ 2 randomized clinical trial. JAMA. 2023;330:512–27. https://doi.org/10.1001/jama.2023.13239
4. Wang YJ. Alzheimer disease: lessons from immunotherapy for Alzheimer disease. Nat Rev Neurol. 2014;10:188–9. https://doi.org/10.1038/nrneurol.2014.44
5. Liu YH, Giunta B, Zhou HD, Tan J, Wang YJ. Immunotherapy for Alzheimer disease: the challenge of adverse effects. Nat Rev Neurol. 2012;8:465–9. https://doi.org/10.1038/nrneurol.2012.118
6. Self WK, Holtzman DM. Emerging diagnostics and therapeutics for Alzheimer disease. Nat Med. 2023;29:2187–99. https://doi.org/10.1038/s41591-023-02505-2
7. Liu J, van Beusekom H, Bu XL, Chen G, Henrique Rosado de Castro P, Chen X, et al. Preserving cognitive function in patients with Alzheimer's disease: The Alzheimer's disease neuroprotection research initiative (ADNRI). Neuroprotection. 2023;1:84–98. https://doi.org/10.1002/nep3.23
8. Busche MA, Eichhoff G, Adelsberger H, Abramowski D, Wiederhold KH, Haass C, et al. Clusters of hyperactive neurons near amyloid plaques in a mouse model of Alzheimer's disease. Science. 2008;321:1686–9. https://doi.org/10.1126/science.1162844
9. Busche MA, Chen X, Henning HA, Reichwald J, Staufenbiel M, Sakmann B, et al. Critical role of soluble amyloid-β for early hippocampal hyperactivity in a mouse model of Alzheimer's disease. Proc Natl Acad Sci USA. 2012;109:8740–5. https://doi.org/10.1073/pnas.1206171109
10. Massimini M, Huber R, Ferrarelli F, Hill S, Tononi G. The sleep slow oscillation as a traveling wave. J Neurosci. 2004;24:6862–70. https://doi.org/10.1523/jneurosci.1318-04.2004
11. Busche MA, Kekuš M, Adelsberger H, Noda T, Förstl H, Nelken I, et al. Rescue of long-range circuit dysfunction in Alzheimer's disease models. Nat Neurosci. 2015;18:1623–30. https://doi.org/10.1038/nn.4137
12. Tononi G, Cirelli C. Sleep and the price of plasticity: from synaptic and cellular homeostasis to memory consolidation and integration. Neuron. 2014;81:12–34. https://doi.org/10.1016/j.neuron.2013.12.025
13. Niknazar H, Malerba P, Mednick SC. Slow oscillations promote long-range effective communication: The key for memory consolidation in a broken-down network. Proc Natl Acad Sci USA. 2022;119:e2122515119. https://doi.org/10.1073/pnas.2122515119
14. Kang JE, Lim MM, Bateman RJ, Lee JJ, Smyth LP, Cirrito JR, et al. Amyloid-beta dynamics are regulated by orexin and the sleep-wake cycle. Science. 2009;326:1005–7. https://doi.org/10.1126/science.1180962
15. Fultz NE, Bonmassar G, Setsompop K, Stickgold RA, Rosen BR, Polimeni JR, et al. Coupled electrophysiological, hemodynamic, and cerebrospinal fluid oscillations in human sleep. Science. 2019;366:628–31. https://doi.org/10.1126/science.aax5440
16. Xie L, Kang H, Xu Q, Chen MJ, Liao Y, Thiyagarajan M, et al. Sleep drives metabolite clearance from the adult brain. Science. 2013;342:373–7. https://doi.org/10.1126/science.1241224
17. Vyazovskiy VV, Harris KD. Sleep and the single neuron: the role of global slow oscillations in individual cell rest. Nat Rev Neurosci. 2013;14:443–51. https://doi.org/10.1038/nrn3494
18. Mander BA, Marks SM, Vogel JW, Rao V, Lu B, Saletin JM, et al. β-amyloid disrupts human NREM slow waves and related hippocampus-dependent memory consolidation. Nat Neurosci. 2015;18:1051–7. https://doi.org/10.1038/nn.4035
19. Lucey BP, McCullough A, Landsness EC, Toedebusch CD, McLeland JS, Zaza AM, et al. Reduced non-rapid eye movement sleep is associated with tau pathology in early Alzheimer's disease. Sci Transl Med. 2019;11:eaau6550. https://doi.org/10.1126/scitranslmed.aau6550
20. Zott B, Busche MA, Sperling RA, Konnerth A. What happens with the circuit in Alzheimer's disease in mice and humans? Annu Rev Neurosci. 2018;41:277–97. https://doi.org/10.1146/annurev-neuro-080317-061725
21. Haas H, Panula P. The role of histamine and the tuberomamillary nucleus in the nervous system. Nat Rev Neurosci. 2003;4:121–30. https://doi.org/10.1038/nrn1034
22. Schwartz JC. The histamine H3 receptor: from discovery to clinical trials with pitolisant. Br J Pharmacol. 2011;163:713–21. https://doi.org/10.1111/j.1476-5381.2011.01286.x
23. Medhurst AD, Roberts JC, Lee J, Chen CP, Brown SH, Roman S, et al. Characterization of histamine H3 receptors in Alzheimer's disease brain and amyloid overexpressing TASTPM mice. Br J Pharmacol. 2009;157:130–8. https://doi.org/10.1111/j.1476-5381.2008.00075.x

24. Nomura H, Mizuta H, Norimoto H, Masuda F, Miura Y, Kubo A, et al. Central histamine boosts perirhinal cortex activity and restores forgotten object memories. Biol Psychiatry. 2019;86:230–9. https://doi.org/10.1016/j.biopsych.2018.11.009
25. Oakley H, Cole SL, Logan S, Maus E, Shao P, Craft J, et al. Intraneuronal beta-amyloid aggregates, neurodegeneration, and neuron loss in transgenic mice with five familial Alzheimer's disease mutations: potential factors in amyloid plaque formation. J Neurosci. 2006;26:10129–40. https://doi.org/10.1523/jneurosci.1202-06.2006
26. Nietz AK, Popa LS, Streng ML, Carter RE, Kodandaramaiah SB, Ebner TJ. Wide-field calcium imaging of neuronal network dynamics in vivo. Biology. 2022;11:1601. https://doi.org/10.3390/biology11111601
27. Ren C, Komiyama T. Wide-field calcium imaging of cortex-wide activity in awake, head-fixed mice. STAR Protoc. 2021;2:100973. https://doi.org/10.1016/j.xpro.2021.100973
28. Masters CL, Bateman R, Blennow K, Rowe CC, Sperling RA, Cummings JL. Alzheimer's disease. Nat Rev Dis Primers. 2015;1:15056. https://doi.org/10.1038/nrdp.2015.56
29. Albert MS. Cognitive and neurobiologic markers of early Alzheimer disease. Proc Natl Acad Sci USA. 1996;93:13547–51. https://doi.org/10.1073/pnas.93.24.13547
30. Mueller SM, Arias MG, Mejuto Vázquez G, Schiebener J, Brand M, Wegmann E. Decision support in patients with mild Alzheimer's disease. J Clin Exp Neuropsychol. 2019;41:484–96. https://doi.org/10.1080/13803395.2019.1585517
31. Anacker C, Hen R. Adult hippocampal neurogenesis and cognitive flexibility - linking memory and mood. Nat Rev Neurosci. 2017;18:335–46. https://doi.org/10.1038/nrn.2017.45
32. Vorhees CV, Williams MT. Morris water maze: procedures for assessing spatial and related forms of learning and memory. Nat Protoc. 2006;1:848–58. https://doi.org/10.1038/nprot.2006.116
33. Masters CL, Simms G, Weinman NA, Multhaup G, McDonald BL, Beyreuther K. Amyloid plaque core protein in Alzheimer disease and down syndrome. Proc Natl Acad Sci USA. 1985;82:4245–9. https://doi.org/10.1073/pnas.82.12.4245
34. Herzig MC, Winkler DT, Burgermeister P, Pfeifer M, Kohler E, Schmidt SD, et al. Abeta is targeted to the vasculature in a mouse model of hereditary cerebral hemorrhage with amyloidosis. Nat Neurosci. 2004;7:954–60. https://doi.org/10.1038/nn1302
35. Gowrishankar S, Yuan P, Wu Y, Schrag M, Paradise S, Grutzendler J, et al. Massive accumulation of luminal protease-deficient axonal lysosomes at Alzheimer's disease amyloid plaques. Proc Natl Acad Sci USA. 2015;112:E3699–3708. https://doi.org/10.1073/pnas.1510329112
36. Yuan P, Zhang M, Tong L, Morse TM, McDougal RA, Ding H, et al. PLD3 affects axonal spheroids and network defects in Alzheimer's disease. Nature. 2022;612:328–37. https://doi.org/10.1038/s41586-022-05491-6
37. Lee JH, Yang DS, Goulbourne CN, Im E, Stavrides P, Pensalfini A, et al. Faulty autolysosome acidification in Alzheimer's disease mouse models induces autophagic build-up of Aβ in neurons, yielding senile plaques. Nat Neurosci. 2022;25:688–701. https://doi.org/10.1038/s41593-022-01084-8
38. Tsai J, Grutzendler J, Duff K, Gan WB. Fibrillar amyloid deposition leads to local synaptic abnormalities and breakage of neuronal branches. Nat Neurosci. 2004;7:1181–3. https://doi.org/10.1038/nn1335
39. He C, Luo F, Chen X, Chen F, Li C, Ren S, et al. Superficial layer-specific histaminergic modulation of medial entorhinal cortex required for spatial learning. Cereb Cortex. 2016;26:1590–608. https://doi.org/10.1093/cercor/bhu322
40. Manz KM, Becker JC, Grueter CA, Grueter BA. Histamine H(3) receptor function biases excitatory gain in the nucleus accumbens. Biol Psychiatry. 2021;89:588–99. https://doi.org/10.1016/j.biopsych.2020.07.023
41. Lee S, Sato Y, Nixon RA. Lysosomal proteolysis inhibition selectively disrupts axonal transport of degradative organelles and causes an Alzheimer's-like axonal dystrophy. J Neurosci. 2011;31:7817–30. https://doi.org/10.1523/jneurosci.6412-10.2011
42. Hui L, Soliman ML, Geiger NH, Miller NM, Afghah Z, Lakpa KL, et al. Acidifying Endolysosomes Prevented Low-Density Lipoprotein-Induced Amyloidogenesis. J Alzheimer's Dis. 2019;67:393–410. https://doi.org/10.3233/jad-180941
43. Luo H, Li X, Fan R, Ruan Y, Qian L, Shen Y, et al. Neuroprotective effect of histamine H3 receptor blockade on methamphetamine-induced cognitive impairment in mice. Pharmacol Biochem Behav. 2023;222:173512. https://doi.org/10.1016/j.pbb.2022.173512
44. Leurs R, Bakker RA, Timmerman H, de Esch IJ. The histamine H3 receptor: from gene cloning to H3 receptor drugs. Nat Rev Drug Discov. 2005;4:107–20. https://doi.org/10.1038/nrd1631
45. Coffey EE, Beckel JM, Laties AM, Mitchell CH. Lysosomal alkalization and dysfunction in human fibroblasts with the Alzheimer's disease-linked presenilin 1 A246E mutation can be reversed with cAMP. Neuroscience. 2014;263:111–24. https://doi.org/10.1016/j.neuroscience.2014.01.001
46. Bassetti CLA, Adamantidis A, Burdakov D, Han F, Gay S, Kallweit U, et al. Narcolepsy - clinical spectrum, aetiopathophysiology, diagnosis and treatment. Nat Rev Neurol. 2019;15:519–39. https://doi.org/10.1038/s41582-019-0226-9
47. López-Otín C, Kroemer G. Hallmarks of Health. Cell. 2021;184:33–63. https://doi.org/10.1016/j.cell.2020.11.034
48. Mizushima N, Levine B, Cuervo AM, Klionsky DJ. Autophagy fights disease through cellular self-digestion. Nature. 2008;451:1069–75. https://doi.org/10.1038/nature06639
49. Nixon RA. The role of autophagy in neurodegenerative disease. Nat Med. 2013;19:983–97. https://doi.org/10.1038/nm.3232
50. Boland B, Yu WH, Corti O, Mollereau B, Henriques A, Bezard E, et al. Promoting the clearance of neurotoxic proteins in neurodegenerative disorders of ageing. Nat Rev Drug Discov. 2018;17:660–88. https://doi.org/10.1038/nrd.2018.109
51. Menzies FM, Fleming A, Caricasole A, Bento CF, Andrews SP, Ashkenazi A, et al. Autophagy and neurodegeneration: pathogenic mechanisms and therapeutic opportunities. Neuron. 2017;93:1015–34. https://doi.org/10.1016/j.neuron.2017.01.022
52. Bourdenx M, Martín-Segura A, Scrivo A, Rodriguez-Navarro JA, Kaushik S, Tasset I, et al. Chaperone-mediated autophagy prevents collapse of the neuronal metastable proteome. Cell. 2021;184:2696–714.e2625. https://doi.org/10.1016/j.cell.2021.03.048
53. Fleming A, Bourdenx M, Fujimaki M, Karabiyik C, Krause GJ, Lopez A, et al. The different autophagy degradation pathways and neurodegeneration. Neuron. 2022;110:935–66. https://doi.org/10.1016/j.neuron.2022.01.017
54. Iida T, Yoshikawa T, Matsuzawa T, Naganuma F, Nakamura T, Miura Y, et al. Histamine H3 receptor in primary mouse microglia inhibits chemotaxis, phagocytosis, and cytokine secretion. Glia. 2015;63:1213–25. https://doi.org/10.1002/glia.22812
55. Yan H, Zhang X, Hu W, Ma J, Hou W, Zhang X, et al. Histamine H3 receptors aggravate cerebral ischaemic injury by histamine-independent mechanisms. Nat Commun. 2014;5:3334. https://doi.org/10.1038/ncomms4334
56. Knowles RB, Wyart C, Buldyrev SV, Cruz L, Urbanc B, Hasselmo ME, et al. Plaque-induced neurite abnormalities: implications for disruption of neural networks in Alzheimer's disease. Proc Natl Acad Sci USA. 1999;96:5274–9. https://doi.org/10.1073/pnas.96.9.5274
57. Dan Y, Poo MM. Spike timing-dependent plasticity of neural circuits. Neuron. 2004;44:23–30. https://doi.org/10.1016/j.neuron.2004.09.007
58. Slutsky I. Linking activity dyshomeostasis and sleep disturbances in Alzheimer disease. Nat Rev Neurosci. 2024;25:272–84. https://doi.org/10.1038/s41583-024-00797-y
59. Lüscher C, Malenka RC. NMDA receptor-dependent long-term potentiation and long-term depression (LTP/LTD). Cold Spring Harb Perspect Biol. 2012;4:a005710. https://doi.org/10.1101/cshperspect.a005710
60. Arrang JM, Garbarg M, Schwartz JC. Auto-inhibition of brain histamine release mediated by a novel class (H3) of histamine receptor. Nature. 1983;302:832–7. https://doi.org/10.1038/302832a0
61. Ligneau X, Perrin D, Landais L, Camelin JC, Calmels TP, Berrebi-Bertrand I, et al. BF2.649 [1-{3-[3-(4-Chlorophenyl)propoxy]propyl}piperidine, hydrochloride], a nonimidazole inverse agonist/antagonist at the human histamine H3 receptor: Preclinical pharmacology. J Pharmacol Exp Ther. 2007;320:365–75. https://doi.org/10.1124/jpet.106.111039
62. Zheng Y, Fan L, Fang Z, Liu Z, Chen J, Zhang X, et al. Postsynaptic histamine H(3) receptors in ventral basal forebrain cholinergic neurons modulate contextual fear memory. Cell Rep. 2023;42:113073. https://doi.org/10.1016/j.celrep.2023.113073
63. Stevens TH, Forgac M. Structure, function and regulation of the vacuolar (H+)-ATPase. Annu Rev Cell Dev Biol. 1997;13:779–808. https://doi.org/10.1146/annurev.cellbio.13.1.779
64. Alzamora R, Thali RF, Gong F, Smolak C, Li H, Baty CJ, et al. PKA regulates vacuolar H+-ATPase localization and activity via direct phosphorylation of the a subunit in kidney cells. J Biol Chem. 2010;285:24676–85. https://doi.org/10.1074/jbc.M110.106278
65. Wang J, Liu B, Xu Y, Yang M, Wang C, Song M, et al. Activation of CREB-mediated autophagy by thioperamide ameliorates β-amyloid pathology and cognition in Alzheimer's disease. Aging Cell. 2021;20:e13333. https://doi.org/10.1111/acel.13333
66. Zhang M, Liu LY, Xu Y, Wang WZ, Qiu NZ, Zhang FF, et al. Imbalance of multiple neurotransmitter pathways leading to depression-like behavior and cognitive dysfunction in the triple transgenic mouse model of Alzheimer disease. Metab Brain Dis. 2023;38:2465–76. https://doi.org/10.1007/s11011-023-01242-2
67. Xia P, Logiacco F, Huang Y, Kettenmann H, Semtner M. Histamine triggers microglial responses indirectly via astrocytes and purinergic signaling. Glia. 2021;69:2291–304. https://doi.org/10.1002/glia.24039

ACKNOWLEDGEMENTS

The authors are grateful to Ms. Jia Lou for help in composing and layout editing of the figures. This study was supported by grants from the National Natural Science Foundation of China to X.C. and K.Z. (No. 31925018, 32127801, 82371485), the National Key R&D Program of China (2021YFA0805000) to X.C. and Guangxi Science and Technology Base & Talents Fund (GUIKE AD22035948).

AUTHOR CONTRIBUTIONS

Project design, YZ, YW, Yun.Z, SL, XC; surgery and histology, YZ, JZ; behavioral experiments, YZ, LY, JF, HZ; widefield calcium imaging, YZ, JZ; data interpretation and analysis, YZ, XL, ZY, KZ, CZ, HJ, AK, YW, Yun.Z, SL, XC; figure preparation, YZ, SL, XC; manuscript writing, YZ, Yun.Z, SL, XC All authors read and comment on the manuscript.

COMPETING INTERESTS

The authors declare no competing interests.

ADDITIONAL INFORMATION

Supplementary information The online version contains supplementary material available at https://doi.org/10.1038/s41398-025-03358-8.

Correspondence and requests for materials should be addressed to Chunqing Zhang, Yun Zhang, Sunny C. Li or Xiaowei Chen.